Apparent and effective physical properties of heterogeneous materials: Representativity of samples of two materials from food industry

Toufik Kanit [a], Franck N'Guyen [a], Samuel Forest [a,*], Dominique Jeulin [a,b], Matt Reed [c], Scott Singleton [d]

[a] *Centre des Matériaux, Ecole des Mines de Paris, B.P. 87, 91003 Evry, France*
[b] *Centre de Morphologie Mathématique, Ecole des Mines de Paris, 35, rue St-Honoré, 77305 Fontainebleau, France*
[c] *Unilever Research, Port Sunlight Laboratory, Quarry Road, East Bebington, Wirral L63 3JW, United Kingdom*
[d] *Unilever Research, Colworth House, Sharnbrook, Bedford MK44 1LQ, United Kingdom*

Abstract

Three-dimensional confocal images of two materials A and B from food industry made of two constituents with highly contrasted properties, having the same volume fraction but different morphologies, are used to estimate their effective elastic and thermal properties. For that purpose, finite element simulations based on explicit meshing of the microstructures are performed on six samples of the materials, with different boundary conditions: kinematic uniform (KUBC), stress uniform (SUBC) and periodic boundary conditions. Direct simulations on the entire samples show that KUBC and SUBC provide strongly different apparent properties, which rises the question of the representativity of the samples. A numerical and statistical computational homogenization methodology first proposed for random models of microstructures in [Kanit et al., Determination of the size of the representative volume element for random composites: statistical and numerical approach, Int. J. Solids Struct. 40 (2003) 3647–3679] is extended here to the case of real microstructures in order to estimate the size of representative volume elements (RVE) for both materials. The samples of material A are found to be representative, whereas at least twice as large sample volumes would be necessary to predict the properties of material B with a precision of 5%. Numerical predictions of the effective properties using simulations on a large number of subdomains extracted from the samples with periodic boundary conditions are in satisfactory agreement with available experimental results. In particular, material A is twice as stiff as material B. This is due to a different percolation behaviour of the hard phase in the materials, which is investigated in the last section of the article. Indicators of geometrical and mechanical percolation, especially relevant for connected microstructures, are proposed and estimated using 3D image analysis.
© 2005 Elsevier B.V. All rights reserved.

Keywords: Representative volume element; Homogenization; Elasticity; Thermal conductivity; Percolation; Food material; Ice cream; Finite element; Parallel computing

1. Introduction

The effective physical properties of heterogeneous materials strongly depend on the morphology of phase distribution in space [20,40]. Such microstructural effects are more important when the contrast in the properties of the constituent is high. Much can be done analytically, including bounding and estimation of overall properties, when the composite is made up of

---

* Corresponding author.
E-mail address: Samuel.Forest@ensmp.fr (S. Forest).

inclusions having simple geometries that are embedded in a matrix and as long as the contrast in phase properties is not too high [4,15,39,33]. For higher contrasts, for example in the case of porous materials, the actual morphology of the microstructure plays a dominant role in the final effective property. Modern experimental techniques make it possible to obtain realistic 3D representations of materials microstructures. They include 2D images acquired using electron or light microscopy, 3D images obtained using X-ray microtomography [36], serial sectioning, confocal imaging, or magnetic resonance imaging. These techniques provide the opportunity of directly measuring the complex morphology of the composite materials in 3D at resolutions down to a few microns.

There now exist large-scale computational methods for calculating the properties of heterogeneous materials given a digital representation of their morphology [1,2,14,30,29]. 3D models have also been directly reconstructed from samples by combining digitized serial sections obtained by scanning electron microscopy [23], or using the technique of X-ray microtomography [12,37] and laser confocal microscopy [13]. The number of contributions providing direct links between 3D images and finite element computations remains small but is increasing [26]. This is part of the current effort to develop microstructural mechanics with a view to optimizing microstructures for wanted properties [41,7,42]. The determination of apparent properties goes through the resolution of boundary value problems on samples of microstructures. The resulting apparent properties depend in fact on the choice of boundary conditions used to impose mean strain, stress, thermal gradient or flux. Three types of boundary conditions are classically used in computational homogenization: kinematic uniform (KUBC), stress uniform (SUBC) and periodic boundary conditions. Periodic boundary conditions have been shown in [21] in the case of a two-phase elastic material modeled as a Voronoi mosaics, to provide correct estimations of the effective properties for smaller volumes than KU and SU boundary conditions.

The first objective of the present work is to propose a computational strategy to estimate the RVE size in the case of real two-phase heterogeneous materials. Contrary to the case of random models of microstructures, the number and size of images of the microstructure of an actual engineering material are often limited. This raises additional difficulties to assess the representativity of the samples and to estimate the physical properties, compared to the approach developed in [21]. Two materials made with the same constituents but having significantly different morphologies are studied in this work. Both morphologies exhibit an interconnected character for both phases. The second objective of this work is then to point out a morphological and/or mechanical parameter that makes it possible to distinguish different interconnected microstructures. The proposed parameter is called here the percolation ratio. It will appear that RVE size and percolation ratio are correlated parameters.

In the present work, 3D confocal images of two materials from food industry are used to predict their effective physical properties, namely linear elasticity and thermal conductivity. The two materials, labelled A and B are made of two phases, namely a hard phase, polycrystalline ice, labelled 1, and a soft and less conductive phase, fat product close to cream, labelled 2. Materials from food industry have gained considerable interest from materials science and mechanical engineering community because of the strong links between physical, mechanical and sensorial properties [19]. Although computational homogenization methods were already applied to polycrystalline ice [10], mechanical analyses of ice creams based on actual morphology of microstructures are not reported in literature [6]. The contrasts in the Young's modulus and thermal conductivity between both phases are respectively 1000 and 100. The volume fraction of phase 1 in materials A and B is similar, and close to 70%. Material processing techniques differ for both materials, resulting in strongly different microstructures, a rather fine microstructure for material A, and a coarser one for material B. Special care was taken during material processing in order to avoid the presence of porosities in the mixtures. Isolated pores may exist in the sample but they are not taken into account in the proposed simulations. Experimental tests carried out on both materials show that the overall properties of A and B differ significantly: Young's modulus is found to be twice as high for A as for B. In the present work, the effective elastic and thermal properties are estimated from the available 3D confocal images using computational homogenization techniques. In particular, we try to find out the differences in the morphology of the microstructures that can explain the strongly different elastic behaviour. The attention is drawn on the percolation behaviour of the hard phase inside the mixture. To quantify the precision of the found numerical estimates, the question of the representativity of the finite size samples must be raised and investigated in detail.

The discussion on the estimation of RVE sizes relies on a numerical and statistical approach proposed in [21]. The effective physical properties of random heterogeneous materials can be determined not only by numerical simulations on *large* volume elements of composite, but also as mean values of apparent properties of rather *small* volumes, provided that a sufficient number of realizations of the microstructure is considered. The size V^{RVE} must be considered as a function of several parameters: the physical property, the contrast of properties c, the volume fraction of the constituents, the wanted relative precision ϵ_{rel} for the estimation of the effective property and the number n of realizations of the microstructure associated with computations that one is able to carry out, and of course on the morphology of spatial phase distribution. The size of RVE was related in [21] to the notion of *integral range*, denoted A_3 which depends on the specific morphological or physical property. The integral range is directly related to the scatter in apparent properties found on volumes of fixed size but containing different realizations of the microstructure of a random material. In most cases, it can be determined only numerically for example by finite element simulations, as done in [21] in the case of a random material model, namely

Voronoi mosaics. The integral range is estimated numerically in the present work for the real materials A and B. For that purpose, finite element computations on volumes with increasing sizes extracted from the available samples are performed to determine apparent elastic and thermal properties and their dispersion as a function of domain size. For sufficiently large domains, the mean properties converge towards a single value that is regarded as the effective one.

Section 2 is devoted to the description of the images of the microstructure of materials A and B. The experimental physical properties found for the constituents of the materials and for the materials A and B themselves are presented. Volume fraction and covariance ranges are given for all samples. The computational methods for meshing microstructures and the type of boundary conditions are presented in Section 3. Direct simulations of the elastic and thermal apparent properties of all available samples are provided in Section 4 using KU and SU boundary conditions. The question of the proper RVE size for both materials is discussed in Section 5. Section 6 aims at providing morphological and mechanical arguments justifying why microstructure A leads to stiffer elastic properties and to a more conductive material than microstructure B. The key notion explored is that of percolation of the hard phase within the mixture. Indicators of geometrical and mechanical percolation are defined and estimated using 3D image analysis.

2. Microstructure and properties of the materials

The two investigated materials A and B are made of two phases, labelled 1 (polycrystalline phase, ice) and 2 (fat polymer phase, cream). Experimental batches of the studied composite materials are produced in blocks of 500 g which can be used for four-point bending tests and confocal imaging. Three samples of each material (SA_1, SA_2, SA_3) and (SB_1, SB_2, SB_3) are studied in the present work. Confocal images of samples SA_3 and SB_1 are shown in Fig. 1. The material A contains elongated crystals of phase 1, whereas material B contains fairly round hard phase crystals. The volume fractions of phase 1, called P_1, are given in Table 1 for all the samples. The mean volume fraction $\bar{P}_1$ is 69.3% for the three samples in material A and 72% in material B. The size of the samples is $250 \times 250 \times 30\ \mu m^3$. The shortest dimension is called (OZ). The largest edges are along the directions (OX) and (OY). The dimensions of the samples lead to the image size: $512 \times 512 \times 60 = 15,728,640$ voxels, i.e. a resolution of about: 8 voxels/μm^3.

2.1. Morphological description of the microstructures

It is important to account for the presence of scales, size of heterogeneities, of the components of a microstructure. The basic morphological tools for these aspects are the covariance and covariance range L [27,20]. These parameters are given
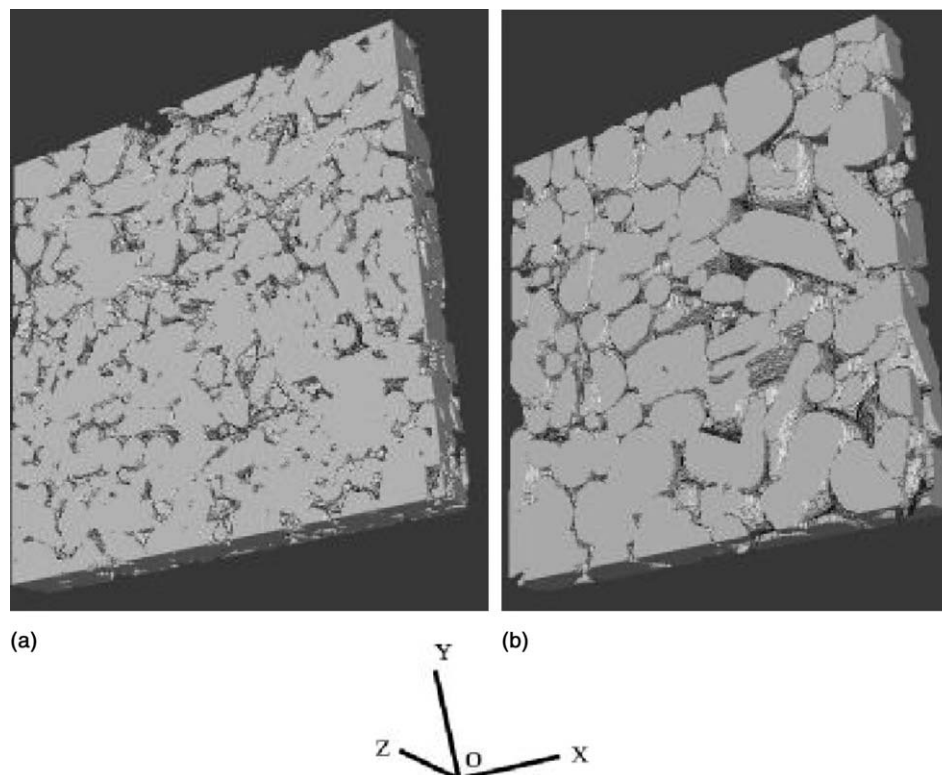

Fig. 1. 3D confocal imaging, the phase 1 is in grey color, the phase 2 is transparent: (a) sample SA_3 and (b) sample SB_1.

Table 1
Volume fraction P_1 of hard phase and the covariance range of materials A and B

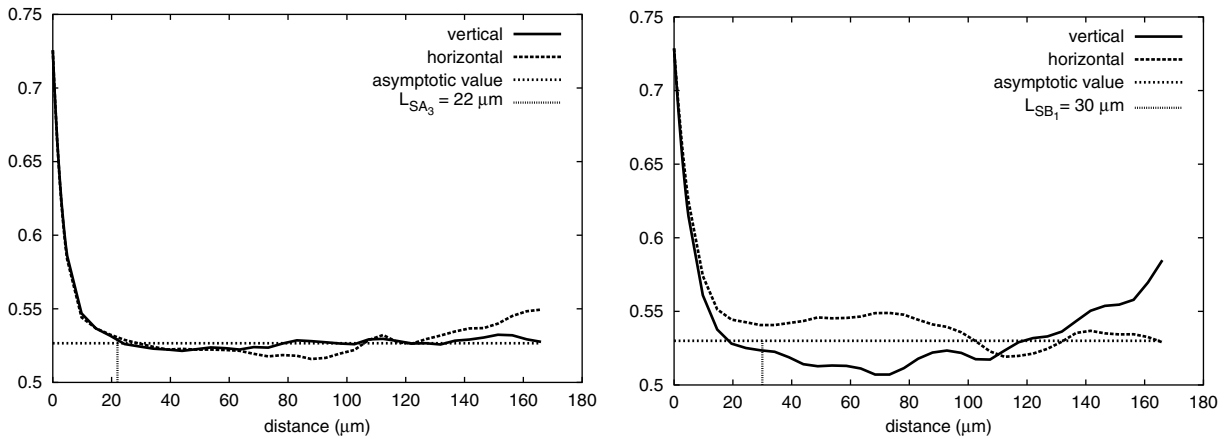|	Samples					
	SA_1	SA_2	SA_3	SB_1	SB_2	SB_3
Covariance range L (µm)	15	14	22	30	26	38
Volume fraction P_1 (%)	66.76	68.64	72.43	73.01	75.19	69.05

Fig. 2. Covariance diagram and covariance range L of sample SA_3 (on the left) and sample SB_1 (on the right), in direction (OX) (called horizontal) and (OY) (called vertical).

for samples SA_3 and SB_1 in Fig. 2. The covariances of the samples are practically equal in both directions of observation (OX, OY). They reach an asymptotic value for a finite range, which measures the scale of the microstructure. A range (for the phase 1) close to: $L_A = 15$ µm is observed in material A and $L_B = 30$ µm in material B (see Table 1). The fairly round hard phase crystals in material B lead to a larger covariance range. The fact that the covariance range L_B of material B is larger than in material A, will have a major influence on the estimated values of RVE size for physical properties in these materials. A model of random microstructure to simulate this kind of microstructures was developed in [6].

2.2. Physical properties

This work deals with the elastic and thermal properties of the investigated materials. These properties are known for the two individual constituents and also for the composite materials. The size of the constituent and the material processing technique is such that it is reasonable to assume that the constituents embedded in the composite material exhibit an isotropic behaviour. The Young's moduli, Poisson ratio and thermal conductivity of phases 1 and 2 are respectively

$$(E_1, v_1, E_2, v_2, \lambda_1, \lambda_2) = (2500, 0.30, 2.5, 0.49, 2.44, 0.0244) \ (\text{MPa}, \text{W m}^{-1} \text{K}^{-1}). \tag{1}$$

These properties correspond respectively to pure polycrystalline ice and pure cream tested at $-18\,°C$. They were determined from four-point bending tests carried out at that temperature.

Homogenization theory provides us with bounds for the effective physical properties (elastic bulk and shear moduli and thermal conductivity) of any mixture of components A and B. The Voigt and Reuss bounds are absolute upper and lower bounds for given volume fraction of the constituents. The Hashin–Shtrikman bounds are used here for isotropic two-phase materials. However, in the present case, these bounds are very far apart because of the very large contrast in the properties of the constituents (cf. the results reported in Table 5):

$$c_E = E_1/E_2 = 1000, \qquad c_\lambda = \lambda_1/\lambda_2 = 100. \tag{2}$$

In this work, we use the Young's moduli based on Hashin–Shtrikman bounds for shear and bulk moduli, $E^{\text{HS}+}$ and $E^{\text{HS}-}$, and given by

$$E^{\text{HS}+} = \frac{9k^{\text{HS}+}\mu^{\text{HS}+}}{3k^{\text{HS}+} + \mu^{\text{HS}+}}, \qquad E^{\text{HS}-} = \frac{9k^{\text{HS}-}\mu^{\text{HS}-}}{3k^{\text{HS}-} + \mu^{\text{HS}-}}, \tag{3}$$

where $k^{\text{HS}+}$ and $k^{\text{HS}-}$ (respectively $\mu^{\text{HS}+}$ and $\mu^{\text{HS}-}$) are the Hashin–Shtrikman bounds for k (respectively μ). The self-consistent estimates are also used to compare experimental and numerical results in this work [34]. For the studied materials (volume fraction $P_1 = 0.7$), these predictions are

$$(E^{\text{SC}} = 1024 \text{ MPa}, \quad \lambda^{\text{SC}} = 1.36 \text{ W m}^{-1} \text{ K}^{-1}). \tag{4}$$

Four-point bending tests were performed to determine experimentally the elastic properties of both composite materials A and B [9]. The results concerning the Young's modulus and the thermal properties (λ_A is not available) are

$$(E_A = 511 \text{ MPa}, \quad E_B = 203 \text{ MPa}, \quad \lambda_B = 0.85 \text{ W m}^{-1} \text{ K}^{-1}), \tag{5}$$

where the thermal conductivity found experimentally for material B from other tests is also given. The isotropy of the found properties can be attributed to the material processing which does not introduce privileged directions of mixing. Material A is found to be significantly stiffer than material B. This difference can be explained by the difference of morphology of phases in each material, since A and B have about the same volume fractions of phase 1 and 2. The self-consistent estimation for elastic properties is closer to the properties of material A than B, but it overestimates it by a factor two. The self-consistent model for thermal conductivity overestimates λ_B.

3. Computational homogenization tools

3.1. Field and constitutive equations

The field equations to be solved numerically in the present work concern the linearized theory of elastic solids, on the one hand, and that of heat transfer, on the other hand. The associated governing equations for a body V are the balance of momentum, on the one hand, and the heat equation on the other hand. They must be fulfilled at any regular material point $\underline{x} \in V$

$$\sigma_{ij,j} = 0, \quad q_{i,i} = 0 \tag{6}$$

in a Cartesian orthonormal coordinate system. The comma $,i$ denotes partial derivation with respect to the coordinate x_i. The components σ_{ij} and q_i denote the stress tensor and the heat flux vector respectively. Sources terms, such as body forces and heat production, are not considered in this work. Dynamical effects and transient thermal conduction are excluded. Both frameworks are considered independently. The problem of thermomechanical coupling is not addressed. The corresponding variational formulations relevant for the resolution of a boundary value problem on V with a set of given boundary conditions, classically read

$$\int_V \sigma_{ij} v_{i,j} \, dV = \int_{\partial V_t} t_i v_i \, dS, \quad \int_V q_i \theta_{,i} \, dV = \int_{\partial V_q} q\theta \, dS. \tag{7}$$

∂V_t (resp. ∂V_q) denotes the part of the boundary ∂V of V where the traction vector $t_i = \sigma_{ij}n_j$ (resp. heat flux $q_i n_i = q$) is prescribed. The virtual displacement field v_i (resp. temperature field θ) with sufficient regularity must vanish on the part of ∂V where displacement (resp. temperature) is prescribed. The specific boundary conditions used in this work are given in the next section.

The constitutive equations of linear elasticity and conductivity read

$$\sigma_{ij}(\underline{x}) = c_{ijkl}(\underline{x})\varepsilon_{ij}(\underline{x}), \quad \text{with} \quad \varepsilon_{ij} = \tfrac{1}{2}(u_{i,j} + u_{j,i}), \tag{8}$$

$$q_i(\underline{x}) = \lambda_{ij}(\underline{x})g_j(\underline{x}), \quad \text{with} \quad g_i = T_{,i}, \tag{9}$$

where u_i, T are the displacement and temperature fields. The four-rank tensor of elastic moduli and the second-rank tensor of thermal conductivity are called c_{ijkl} and λ_{ij} respectively. In the present work, the local properties are assumed to be isotropic. They are random variables but can take only two possible values corresponding to phases 1 or 2. For each considered volume V of the heterogeneous material, the fields c_{ijkl}, λ_{ij} are known according to the underlying microstructure defined in Section 2.

All equations are written within the small perturbation framework, assuming small strains and small temperature gradients.

3.2. Boundary conditions

In this work, three types of boundary conditions to be prescribed on a volume element V are considered. They correspond to classical ones in computational homogenization (see the chapter by P. Suquet in the book [34], and also [21]). They are recalled here in the case of linear elasticity:

- *Kinematic uniform boundary conditions (KUBC)*: The displacement $\underline{u}$ is imposed at point $\underline{x}$ belonging to the boundary ∂V such that

$$u_i = E_{ij}x_j \quad \forall \underline{x} \in \partial V. \tag{10}$$

E_{ij} are the Cartesian components of a given symmetrical second-rank tensor that does not depend on $\underline{x}$. This implies that the mean strain over V is

$$\langle \varepsilon_{ij} \rangle \hat{=} \frac{1}{V} \int_V \varepsilon_{ij} \, \mathrm{d}V = E_{ij}. \tag{11}$$

The macroscopic stress tensor Σ_{ij} is then defined by the spatial average:

$$\Sigma_{ij} \hat{=} \langle \sigma_{ij} \rangle = \frac{1}{V} \int_V \sigma_{ij} \, \mathrm{d}V. \tag{12}$$

- *Static uniform boundary conditions (SUBC)*: The traction vector is prescribed at the boundary

$$\sigma_{ij}n_j = \Sigma_{ij}n_j \quad \forall \underline{x} \in \partial V \tag{13}$$

Σ_{ij} is a given symmetrical second-rank tensor independent of $\underline{x}$. The vector normal to ∂V at $\underline{x}$ is denoted by $\underline{n}$. This implies that

$$\langle \sigma_{ij} \rangle = \frac{1}{V} \int_V \sigma_{ij} \, \mathrm{d}V = \Sigma_{ij}. \tag{14}$$

The macroscopic strain tensor is then defined as the spatial average:

$$E_{ij} \hat{=} \langle \varepsilon_{ij} \rangle = \frac{1}{V} \int_V \varepsilon_{ij} \, \mathrm{d}V. \tag{15}$$

- *Periodicity boundary conditions*: The displacement field over the entire volume V takes the form

$$u_i = E_{ij}x_j + v_i \quad \forall \underline{x} \in V, \tag{16}$$

where the fluctuation $\underline{v}$ is periodic. It takes the same value at two homologous points on opposite faces of V. The traction vector $\sigma_{ij}n_j$ takes opposite values at two homologous points on opposite faces of V. It is shown for instance in [5] that these periodic conditions imply that

$$\int_V \sigma_{ij}v_{i,j} \, \mathrm{d}V = 0, \quad \text{and} \quad \langle \varepsilon_{ij} \rangle = E_{ij}. \tag{17}$$

The overall stress tensor is then computed as (12).

The three types of boundary conditions are such that the Hill–Mandel condition, that relates the local and global work of internal forces, is automatically fulfilled:

$$\langle \sigma_{ij}\varepsilon_{ij} \rangle = \langle \sigma_{ij} \rangle \langle \varepsilon_{ij} \rangle = \Sigma_{ij}E_{ij}. \tag{18}$$

This condition is at the root of the energetic definition of effective mechanical properties [5].
Similar boundary conditions are used for the problem of thermal conduction in the volume V:

- The conditions of uniform gradient of temperature at the boundary (UGT), amount to prescribing the temperature at any point $\underline{x} \in \partial V$

$$T = G_j x_j \Rightarrow \langle T_{,i} \rangle = G_i, \tag{19}$$

where G_i is a given constant temperature gradient. The overall heat flux is then defined by

$$Q_i \hat{=} \langle q_i \rangle. \tag{20}$$

- According to the dual conditions, called uniform heat flux at the boundary (UHF), the heat flux at any point $\underline{x} \in \partial V$ is given by

$$q_i n_i = Q_i n_i \Rightarrow \langle q_i \rangle = Q_i, \tag{21}$$

where Q_i is the macroscopic heat flux.
- The periodic conditions state that the temperature field takes the form

$$T = G_i x_i + t \quad \forall \underline{x} \in V \Rightarrow \langle T_{,i} \rangle = G_i. \tag{22}$$

The fluctuation temperature t is periodic. The heat flux $q_i n_i$ is antiperiodic. The macroscopic heat flux is then computed using (20).

The three kind of boundary conditions are such that there is the following relationship relating the macro and micro energy dissipations:

$$\langle q_i T_{,i} \rangle = \langle q_i \rangle \langle T_{,i} \rangle = Q_i G_i. \tag{23}$$

3.3. Meshing microstructures

The so-called *multiphase-element technique* is used to superimpose a finite element mesh on the 3D images of the microstructures [25,3,44]. For each integration point of a regular finite element mesh having the size of the considered sample, the closest voxel in the image is determined and the corresponding material property is attributed to it. The used elements are quadratic bricks (20 nodes) with complete integration (27 Gauss points). As a result, different material properties can be encountered inside some elements. The previous references show that this simple meshing strategy leads to correct evaluations of mean stresses and strains inside the phases when compared to proper meshing of interfaces by nodes. On the other hand, a relatively large number of elements is required to obtain the convergence of local results close to interfaces.

Bounds for the errors introduced by the use of multiphase elements and improvement methods of the quality of the integration can be found in [43]. In particular, these authors propose to increase the number of integration points up to $5 \times 5 \times 5$ inside each multiphase elements. In the present work we keep the classical full integration by $3 \times 3 \times 3$. Results presented in [43] also indicate that quadratic interpolation does not significantly improve the convergence of multiphase elements compared to linear ones. In the present work, we use quadratic elements for all homogeneous (one-phase) and multiphase elements, which provides better convergence at least in the homogeneous elements.

Examples of the performance of theses elements in the present situations are given below, together with the strategy for determining the suitable mesh density. Two meshes are shown in Fig. 3 together with the original image.

3.3.1. Global convergence

The studied parameter is the mesh density defined as the volume of material represented by one finite element. Fig. 4 shows the results of computations of Young's modulus E as a function of the number of degrees of freedom used to mesh the sample SA$_2$. A vertical displacement is applied at the top of the sample and fixed to zero at the bottom. The ratio of the mean axial stress component to the mean axial strain component provides the apparent modulus E for each mesh. The material properties of the constituents are given by (1). The number of degrees of freedom was changed from 30,000 to 1,150,000. The number of finite elements was changed from 4096 to 88,200 which means that the mesh density was changed from 458 to 20 μm^3/element. The result is compared to the Voigt and Reuss bounds and also to the self-consistent estimate. Fig. 4 shows that the apparent Young's modulus first rapidly decreases for finer meshes and tends then to stabilize for large numbers of degrees of freedom.

3.3.2. Local convergence

The convergence of the results at the local level must also be checked to make the proper choice for the mesh density. The maps of the equivalent strain ε_{eq} for tension in samples SA$_1$ and SB$_1$ are given in Fig. 3 (mesh density 20 μm^3 per element). It is defined by the equation

$$\varepsilon_{eq} = \sqrt{\varepsilon_{11}^2 + \varepsilon_{22}^2 + \varepsilon_{33}^2 + 2\varepsilon_{12}^2 + 2\varepsilon_{23}^2 + 2\varepsilon_{31}^2}. \tag{24}$$

The strain field is strongly heterogeneous with maximum strain values found in the soft phase. The computation of sample SA$_2$ was performed for different mesh densities. A displacement component along one edge of the parallelepipedic sample parallel to the tensile direction is plotted in Fig. 5 for different mesh densities. Convergence is not totally achieved close to some interfaces where even finer meshes would be necessary to properly account for strong gradients.

As a result of convergence results, a mesh density of 20 μm^3 per element was adopted for all simulations of this work. The found required mesh density leads to a large number of degrees of freedom (displacement or temperature). The size of the elasticity problems dealt with in Section 4 is of 1,200,000 degrees of freedom. To solve efficiently this linear system, a parallel algorithm based on the FETI method was used. The reader is referred to [11,7] for a presentation of the parallel strategy. Thirty-two processors were used for the simulations of the present work.

3.4. Apparent vs effective properties

Finite element computations on a finite size volume of heterogeneous materials provide apparent properties that can now be defined. The tensor of apparent elastic properties C_{ijkl}^{app} relates the macroscopic strain tensor E_{ij} and the macroscopic stress tensor Σ_{ij} by
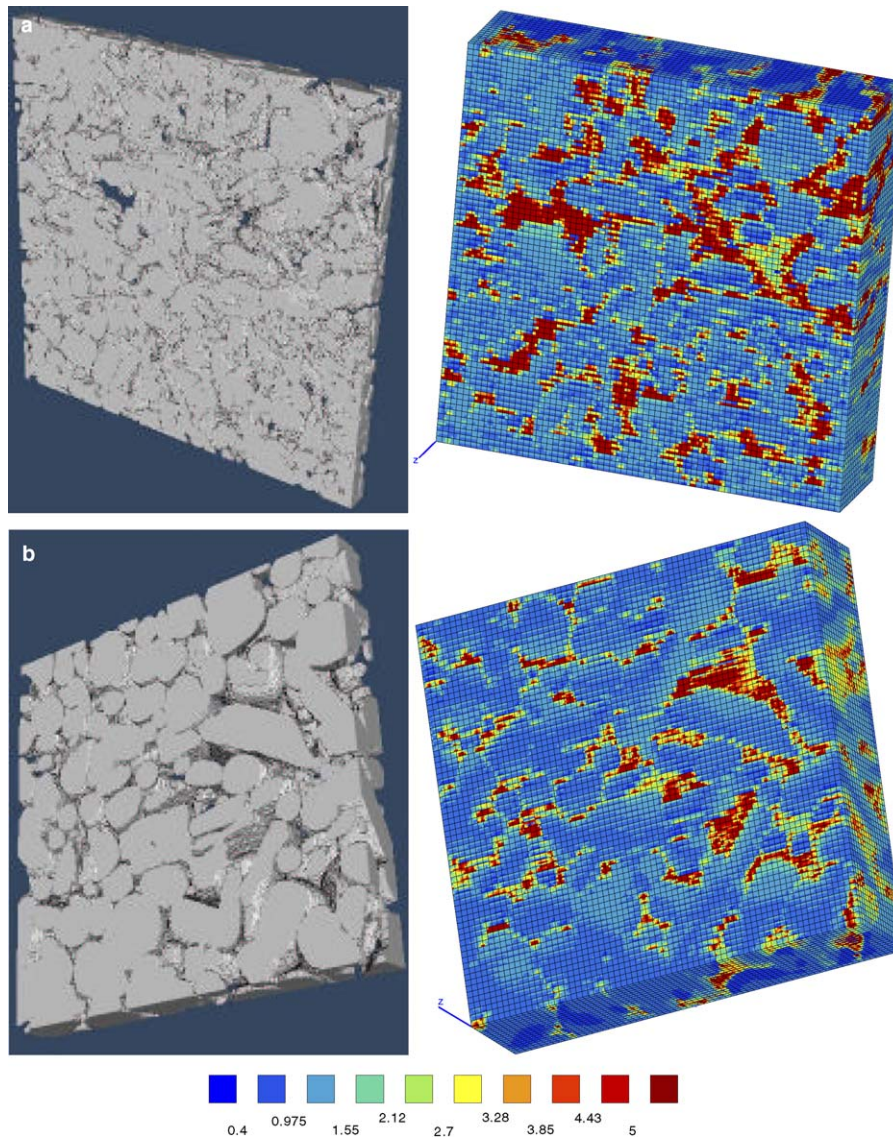
Fig. 3. Mesh and computation with 88,200 elements (1,126,131 degrees of freedom), or 22 μm³/element and map of equivalent strain. (a) The sample SA₁ and (b) the sample SB₁.

$$\Sigma_{ij} = \langle \sigma_{ij} \rangle = C_{ijkl}^{\mathrm{app}} E_{kl}. \tag{25}$$

The tensor E_{ij} and Σ_{ij} are respectively average strain and stress values over the considered sample. Similarly, the tensor of apparent thermal conductivity can be defined for each material volume subjected to a mean temperature gradient of mean heat flux:

$$Q_i = \langle q_i \rangle = \lambda_{ij} G_j. \tag{26}$$

The apparent properties generally depend on the choice of boundary conditions applied to the considered volumes. Huet has derived bounding relationships between the apparent properties obtained from homogeneous boundary conditions [17,16]. Such relations are helpful for checking the validity of the computed results and to interpret the ranking of the apparent properties found in this work for different volume sizes. Primarily, the apparent properties computed on a given volume V based on homogeneous boundary conditions rank as follows:

$$C_{\mathrm{SUBC}}^{\mathrm{app}} \leqslant C_{\mathrm{KUBC}}^{\mathrm{app}}, \qquad \lambda_{\mathrm{UHF}}^{\mathrm{app}} \leqslant \lambda_{\mathrm{UGT}}^{\mathrm{app}}. \tag{27}$$

If the volume V is decomposed into p non-overlapping subvolumes V^i, the reunion of which being equal to V itself, one can determine the apparent property C_i^{app}, λ_i^{app} of each V^i for each type of homogeneous boundary conditions. The mean values of the p apparent properties are denoted by $\overline{C^{\mathrm{app}}}$, $\overline{\lambda^{\mathrm{app}}}$ and can be compared to the apparent property C^{app}, λ^{app} of the large volume V itself:
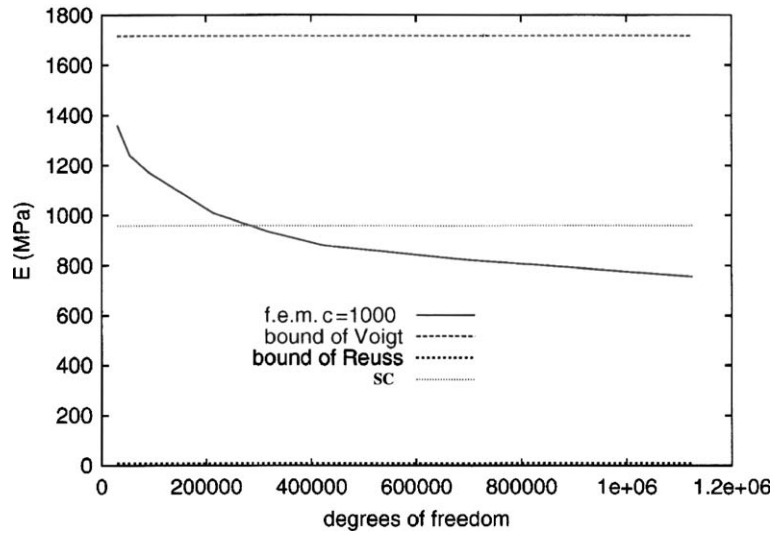
Fig. 4. Effect of the mesh density in finite element simulations on the global convergence of the apparent Young's modulus. c represents the contrast in the Young's moduli of the phases. SC stands for self-consistent model.
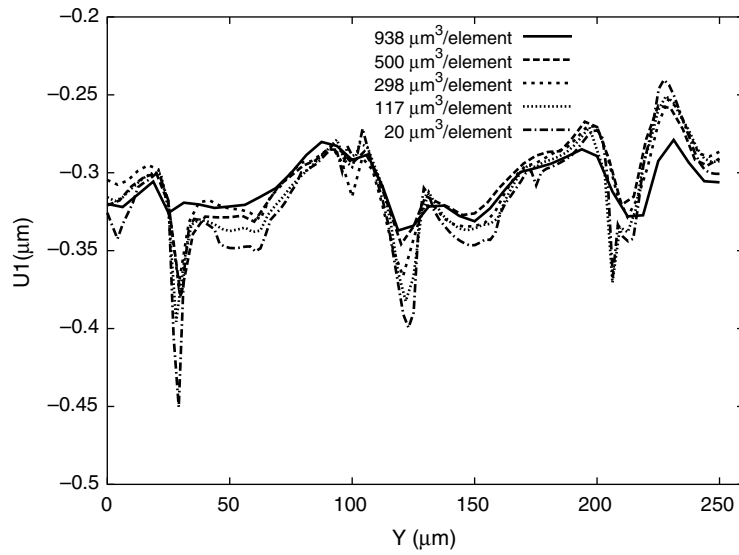

Fig. 5. Effect of mesh density on the local convergence. The displacement component $U1$ along a line on the mesh is plotted for different mesh densities. The mesh density used in the paper is 20 μm^3 per element.

$$\overline{C_{\text{KUBC}}^{\text{app}}} = \frac{1}{p} \sum_{i=1,p} C_{\text{KUBC},i}^{\text{app}}, \quad \overline{C_{\text{SUBC}}^{\text{app}}} = \frac{1}{p} \sum_{i=1,p} C_{\text{KUBC},i}^{\text{app}}, \tag{28}$$

$$\overline{\lambda_{\text{UGT}}^{\text{app}}} = \frac{1}{p} \sum_{i=1,p} \lambda_{\text{UGT},i}^{\text{app}}, \quad \overline{\lambda_{\text{UHF}}^{\text{app}}} = \frac{1}{p} \sum_{i=1,p} \lambda_{\text{UHF},i}^{\text{app}}, \tag{29}$$

$$\overline{C_{\text{SUBC}}^{\text{app}}} \leqslant C_{\text{SUBC}}^{\text{app}} \leqslant C_{\text{KUBC}}^{\text{app}} \leqslant \overline{C_{\text{KUBC}}^{\text{app}}}, \tag{30}$$

$$\overline{\lambda_{\text{UHF}}^{\text{app}}} \leqslant \lambda_{\text{UHF}}^{\text{app}} \leqslant \lambda_{\text{UGT}}^{\text{app}} \leqslant \overline{\lambda_{\text{UGT}}^{\text{app}}}. \tag{31}$$

If the considered volume V is large enough, its apparent properties do not depend on the choice of boundary conditions any longer and coincide therefore with the wanted effective properties C^{eff}, λ^{eff} [31]. As a result, we have

$$\overline{C_{\text{SUBC}}^{\text{app}}} \leqslant C^{\text{eff}} \leqslant \overline{C_{\text{KUBC}}^{\text{app}}}, \quad \overline{\lambda_{\text{UHF}}^{\text{app}}} \leqslant \lambda^{\text{eff}} \leqslant \overline{\lambda_{\text{UGT}}^{\text{app}}}. \tag{32}$$

This result means that the computational homogenization method on limited volumes of heterogeneous material can be used to bound or estimate the wanted effective properties. Finally, the previous quantities can be compared to the Voigt–Reuss/Wiener upper and lower bounds:

$$C^{\text{Reuss}} \leqslant \overline{C^{\text{app}}_{\text{SUBC}}} \leqslant C^{\text{eff}} \leqslant \overline{C^{\text{app}}_{\text{KUBC}}} \leqslant C^{\text{Voigt}}, \tag{33}$$

$$\lambda^{\text{Wiener}-} \leqslant \overline{\lambda^{\text{app}}_{\text{UHF}}} \leqslant \lambda^{\text{eff}} \leqslant \overline{\lambda^{\text{app}}_{\text{UGT}}} \leqslant \lambda^{\text{Wiener}+}. \tag{34}$$

These facts will be illustrated at several places in the simulations of the next sections.

These inequalities are written in the sense of quadratic forms. Similar relations can be written for elastic compliances and heat resistivity.

Similar results are not available in the case of periodicity conditions. However, the apparent properties found using periodicity conditions on volumes of different sizes will be compared systematically to the ones obtained by homogeneous conditions.

4. Determination of apparent properties

4.1. Direct estimation of elastic and thermal properties of sample SA_1 to SB_3

The finite element meshes designed in Section 3.3 are used to compute elastic and thermal apparent properties of the samples SA_1, SA_2, SA_3, SB_1, SB_2, SB_3 introduced in Section 2.

A matrix notation is used to represent the tensor of elastic moduli

$$\begin{pmatrix} \Sigma_{11} \\ \Sigma_{22} \\ \Sigma_{33} \\ \Sigma_{12} \\ \Sigma_{23} \\ \Sigma_{31} \end{pmatrix} = \begin{pmatrix} C^{\text{app}}_{11} & C^{\text{app}}_{12} & C^{\text{app}}_{13} & C^{\text{app}}_{14} & C^{\text{app}}_{15} & C^{\text{app}}_{16} \\ & C^{\text{app}}_{22} & C^{\text{app}}_{23} & C^{\text{app}}_{24} & C^{\text{app}}_{25} & C^{\text{app}}_{26} \\ & & C^{\text{app}}_{33} & C^{\text{app}}_{34} & C^{\text{app}}_{35} & C^{\text{app}}_{36} \\ & & & C^{\text{app}}_{44} & C^{\text{app}}_{45} & C^{\text{app}}_{46} \\ & & & & C^{\text{app}}_{55} & C^{\text{app}}_{56} \\ & & & & & C^{\text{app}}_{66} \end{pmatrix} \begin{pmatrix} E_{11} \\ E_{22} \\ E_{33} \\ 2E_{12} \\ 2E_{23} \\ 2E_{31} \end{pmatrix}. \tag{35}$$

The 6×6 matrix of elastic moduli is symmetrical. The apparent elastic properties depend in general on the choice of boundary conditions [18]. The apparent properties obtained by applying the KUBC boundary conditions (10) to the six samples of the study are given in Table 2. For that purpose, six boundary value problems were solved for each sample. In each boundary value problem, one component of the prescribed strain tensor E_{ij} was set to one, the remaining components being set to zero. The six components of the computed mean stress tensor then provide six coefficients of the matrix of apparent elastic moduli. All components are given in the Cartesian coordinate frame (OX, OY, OZ) defined in Fig. 1.

The found apparent moduli depart from purely isotropic elastic tensors. The coefficients C^{app}_{11} and C^{app}_{22} (in the directions (OX) and (OY)) are very close for all samples. But they are significantly different from the value C^{app}_{33} in the direction (OZ) which appears to be stiffer. Similarly, $C^{\text{app}}_{23} \simeq C^{\text{app}}_{31}$ differs from C^{app}_{12}. To quantify more precisely the anisotropy, the following anisotropy parameters are introduced:

$$a = \frac{2Y_{44}}{Y_{11} - Y_{12}}, \quad \text{with} \quad Y_{44} = \frac{C^{\text{app}}_{44} + C^{\text{app}}_{55} + C^{\text{app}}_{66}}{3},$$

$$Y_{11} = \frac{C^{\text{app}}_{11} + C^{\text{app}}_{22} + C^{\text{app}}_{33}}{3}, \quad Y_{12} = \frac{C^{\text{app}}_{12} + C^{\text{app}}_{23} + C^{\text{app}}_{31}}{3}, \tag{36}$$

$$a_{XY} = \frac{2C^{\text{app}}_{44}}{C^{XY}_{11} - C^{\text{app}}_{12}}, \quad C^{XY}_{11} = \frac{C^{\text{app}}_{11} + C^{\text{app}}_{22}}{2}. \tag{37}$$

The coefficient a is equal to 1 if the elastic behaviour is isotropic. The coefficient a_{XY} is an indicator of in-plane isotropy within the plane (OX, OY). The values of these parameters for all the samples are given in Table 3. They show that a_{XY} remains very close to 1 whereas a significantly departs from 1. This confirms that the behaviour in direction (OZ) is different from that in the (OX, OY) plane. Since no anisotropy is observed at the macroscopic scale, it turns out that the rather small thickness of the samples introduces a bias in the determination of effective properties of the materials. The boundary layer associated with the KUBC boundary conditions affects a significant proportion of the thickness of the sample. The KUBC conditions are known to produce stiffer results than SUBC and periodic conditions according to [17,28,21]. This may explain why the samples are found to be stiffer in the direction (OZ). Note that for sufficiently large volumes, KUBC, SUBC and periodic conditions provide apparent properties converging towards the effective ones [31].

Table 2
Apparent elastic moduli of the six samples of materials A and B investigated in this work

$$C_{SA_1}^{app} = \begin{pmatrix} 904 & 249 & 315 & -1 & 1 & 15 \\ & 813 & 290 & -1 & 5 & 3 \\ & & 1383 & -4 & 7 & 24 \\ & & & 301 & 3 & 1 \\ & & & & 363 & -2 \\ & & & & & 385 \end{pmatrix} \qquad C_{SA_2}^{app} = \begin{pmatrix} 1152 & 352 & 415 & 0 & 0 & 6 \\ & 1098 & 401 & -7 & 5 & 1 \\ & & 1597 & -1 & 9 & 12 \\ & & & 377 & 3 & 2 \\ & & & & 444 & -1 \\ & & & & & 451 \end{pmatrix}$$

$$C_{SA_3}^{app} = \begin{pmatrix} 674 & 166 & 16 & 1 & 0 & 1 \\ & 692 & 163 & 19 & 0 & 0 \\ & & 64 & 0 & 0 & 1 \\ & & & 258 & 0 & -1 \\ & & & & 228 & 0 \\ & & & & & 228 \end{pmatrix} \qquad \overline{C_{SA_m}^{app}} = \begin{pmatrix} 910 & 256 & 249 & 0 & 0 & 7 \\ & 868 & 285 & 4 & 3 & 1 \\ & & 1015 & -2 & 5 & 12 \\ & & & 312 & 2 & 1 \\ & & & & 345 & -1 \\ & & & & & 355 \end{pmatrix}$$

$$C_{SB_1}^{app} = \begin{pmatrix} 1197 & 333 & 416 & -1 & 12 & 23 \\ & 1060 & 384 & 5 & 20 & 7 \\ & & 1675 & 1 & 37 & 34 \\ & & & 387 & 12 & 0 \\ & & & & 457 & 1 \\ & & & & & 489 \end{pmatrix} \qquad C_{SB_2}^{app} = \begin{pmatrix} 1998 & 958 & 966 & 13 & 0 & 11 \\ & 1985 & 960 & 5 & -4 & -1 \\ & & 2215 & 2 & -5 & 16 \\ & & & 500 & 3 & -1 \\ & & & & 537 & 2 \\ & & & & & 545 \end{pmatrix}$$

$$C_{SB_3}^{app} = \begin{pmatrix} 1739 & 859 & 860 & 1 & 5 & 14 \\ & 1661 & 864 & -8 & 29 & 2 \\ & & 1846 & 2 & 25 & 22 \\ & & & 401 & 9 & 13 \\ & & & & 442 & 1 \\ & & & & & 442 \end{pmatrix} \qquad \overline{C_{SB_m}^{app}} = \begin{pmatrix} 1645 & 717 & 747 & 4 & 6 & 16 \\ & 1569 & 736 & 1 & 15 & 3 \\ & & 1912 & 2 & 19 & 24 \\ & & & 429 & 8 & 4 \\ & & & & 479 & 1 \\ & & & & & 492 \end{pmatrix}$$

The matrix $\overline{C}^{app}$ are defined as the mean value of the results obtained from three samples (KUBC boundary conditions).

Table 3
The index of anisotropy of each sample and of the mean matrix of each type

	Samples							
	SA_1	SA_2	SA_3	SA_m	SB_1	SB_2	SB_3	SB_m
a	0.934	0.950	1.316	1.010	0.952	0.954	0.966	0.956
a_{XY}	0.988	0.975	0.998	0.988	0.973	0.968	0.954	0.964

In-plane Young's moduli can be deduced from the coefficients of the elasticity matrices obtained using KUBC (cf. Table 2). They read

$$E_{SA_m}^{KUBC} = 821 \text{ MPa}, \qquad E_{SB_m}^{KUBC} = 1219 \text{ MPa}. \tag{38}$$

These results strongly overestimate the experimental results (5). They even predict that material B is stiffer than A, which is the reverse according the experiment.

The SUBC conditions have been used also to estimate directly the apparent Young's moduli of sample SA_2 and SB_1 in direction (OY). The found values

$$E_{SA_2}^{app} = 754 \text{ MPa}, \qquad E_{SB_1}^{app} = 232 \text{ MPa} \tag{39}$$

depart respectively from 45% and 14% from the experimental values (5). They represent therefore a fair estimation of the experimental properties. In particular, the finite element simulations predict correctly that material A is more than 2.5 times stiffer than material B. The Young's moduli computed by SUBC strongly differ from those obtained with KUBC (38).

The overall thermal conductivity was also determined on the entire samples using UGT and UHF boundary conditions. These tensors are found to be close to isotropic tensors with the following values of apparent thermal conductivity:

$$\lambda_{\text{SA}_2}^{\text{UGT}} = 1.234 \text{ W m}^{-1} \text{ K}^{-1}, \quad \lambda_{\text{SA}_2}^{\text{UHF}} = 1.017 \text{ W m}^{-1} \text{ K}^{-1}, \tag{40}$$

$$\lambda_{\text{SB}_1}^{\text{UGT}} = 1.208 \text{ W m}^{-1} \text{ K}^{-1}, \quad \lambda_{\text{SB}_1}^{\text{UHF}} = 0.765 \text{ W m}^{-1} \text{ K}^{-1}. \tag{41}$$

For the thermal conductivity, the experimental value is available only for the material B. The experimental value $\lambda_{\text{B}} = 0.8 \text{ W m}^{-1} \text{ K}^{-1}$ lies between the obtained bounds $\lambda_{\text{SB}_1}^{\text{UHF}}$ and $\lambda_{\text{SB}_1}^{\text{UGT}}$. Simulations on the whole samples using periodic boundary conditions could not be performed because of the huge amount of additional memory required by these conditions.

Accordingly, direct simulations on small material samples provide fair estimates of the effective properties and predict correctly the ranking between both materials, in the case of SUBC, UHF and UGT boundary conditions. However, the precision of the result is difficult to assess at this stage. In particular, the found anisotropy in the matrices of elastic moduli, and the strong difference between KUBC and SUBC conditions suggest that the considered volumes are not representative enough of the considered materials. This motivates the subsequent developments of this work.

4.2. Quantifying the representativity of the investigated samples

The strongly different results obtained using KU or SU boundary conditions suggest that the samples SA_i and SB_i may not be representative of the materials A and B. Since no larger images of the microstructures are available, the only way of quantifying the distance of the considered samples from an actual RVE size is to work on subvolumes cut inside the samples. The apparent properties found on smaller volumes using different boundary conditions can be compared to the values found for the whole samples. This is part of a strategy initiated by [17,16] and continued by a statistical approach in [21].

Fig. 6 shows the comparison of the strain field in sample SB_1 for the whole sample and for a collection of 16 subvolumes of the sample. The 16 volumes represent a regular non-overlapping partition of the entire sample, as defined in [17]: their intersection is empty and they build up the entire volume SB_1. In the computations, the same SUBC conditions are applied to the whole volume, on the one hand, and to all individual subvolumes, on the other hand. As a result, traction vectors are continuous between two neighboring subvolumes, while the displacement field is not compatible at the boundary between two subvolumes. It can be clearly seen that the boundary layer effects perturb the continuity of large deformation bands developing within the soft phase. Fig. 7 gives the mean value and the scatter of the apparent Young's moduli in direction (OY) for a partition of SA_2 into 4 and 16 regular subvolumes, using SUBC. One can clearly notice the *bias* existing when computing with smaller samples, in comparison with the obtained result on the whole specimen. It turns out that the average value of the apparent Young's moduli computed with SUBC and with a set of smaller samples, forming a uniform partition of the whole specimen, underestimates the apparent Young's modulus estimated on the whole specimen with the same boundary conditions.

The scatter of found apparent properties is also a measure of the loss of representativity when considering smaller volumes. The 16 subvolumes provide 16 apparent Young's moduli with a significant scatter. The difference between the mean value for 16 subvolumes and the apparent Young's modulus of the whole sample is 20%. This technique of regular partition of a large volume was used in [44] as a method to reduce computation time for large-scale finite element computations.

More general results are obtained in the next section using periodic boundary conditions.

5. Effective properties and RVE sizes

The overall physical properties are studied in this part for a large range of volume sizes V and a large number n of small volumes taken out of the whole real specimens of microstructures SA_i and SB_j. Such volumes can be regular subvolumes of the sample as shown in Section 4.2. Smaller volumes were also extracted randomly from the sample and do not represent a partition of the original sample. To some extent, such random volumes represent different realizations of the studied random material. The size and number of considered volumes are given in Table 4. The investigated physical properties are the elastic moduli (bulk modulus k and shear modulus μ) and the thermal conductivity λ.

For each property, the dispersion of the results when increasing the volume V and the integral ranges are reported in Section 5.1. The objective is then to estimate the apparent physical properties (k^{app}, μ^{app}, E^{app} and λ^{app}), as a function of the size of the domain V taken in these microstructures. The mathematical parameter characterizing the dispersion of the found apparent properties, namely the integral range, is identified in the Section 5.2. Quantitative determination of RVE sizes follows in Section 5.3.
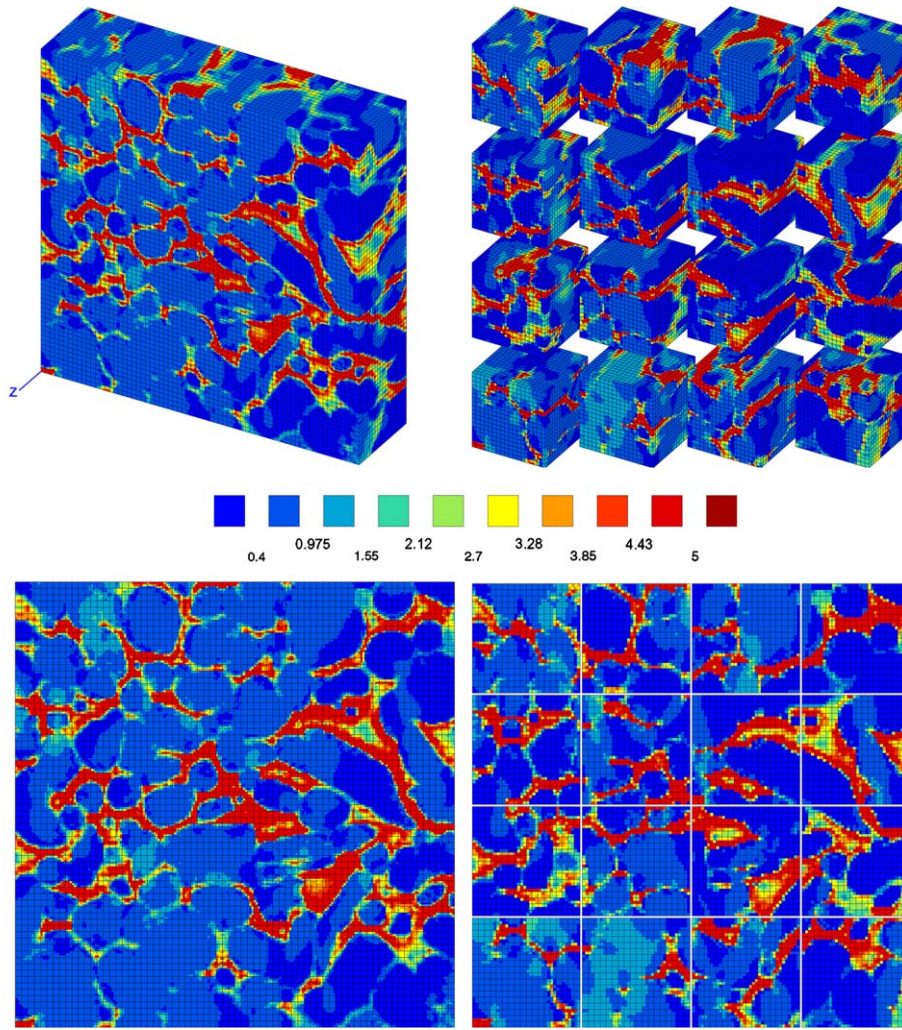
Fig. 6. Application of SUBC on sample SB_1 (applied stress $\Sigma_{22} = 250$ MPa): effect of a regular partition of the volume on the local field of equivalent strain. The whole sample is on the left and the results found for the collection of 16 subvolumes are given on the right.
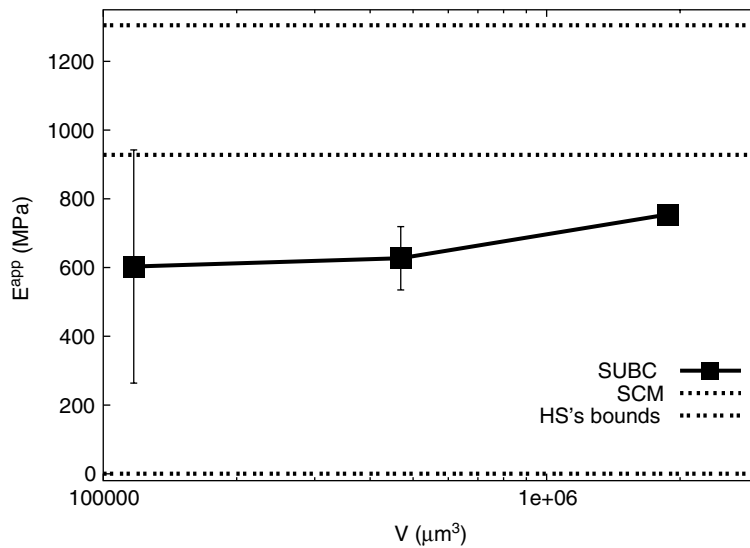

Fig. 7. Mean values and intervals of variation on the mean value for Young's modulus E^{app}, as a function of the domain size for the specimen SA_2 (regular partition of the sample into 1, 4 and 16 subdomains).

Table 4
Number of fields n used for all considered domain sizes, regular and random partitions

Volume of the domain V (μm^3)	Number of fields n
512 (random)	3662
4096 (random)	458
13,824 (random)	136
32,768 (random)	58
117,188 (regular)	16
468,750 (regular)	4
1,875,000 (the whole microstructure)	1

5.1. Dispersion of physical properties

5.1.1. Elastic properties

The numerical simulations based on the finite element method are carried out for two different boundary conditions: KUBC and periodicity conditions for k and μ. The studied specimens are SA$_2$ (as an example of material A) and SB$_1$ (as an example of material B). The chosen number of fields (smaller volumes) n for each sample is such that the product of the small volumes by the n yields the entire volume of the sample (Table 4). For example, the number n of fields for the volume $V = 512$ μm^3 is 3662 fields. They are obtained from regular non-overlapping or random (overlapping) subdivisions of the whole microstructure. In the case of random distributions, the number n of considered volumes must be such that the relative precision on the mean is below a chosen relative precision of 5%, estimated by usual sampling theory. The numbers given in Table 4 were checked to fulfill this condition.

The apparent bulk and shear moduli are determined by applying respectively an overall strain matrix $E_{ij} = \delta_{ij}$ and $E_{ij} = 1/2(\delta_{i1}\delta_{j2} + \delta_{i2}\delta_{j1})$ and computing then the elastic strain energy (see [21] for the complete procedure). Fig. 8 gives the obtained mean values and variances of the apparent moduli k^{app}, μ^{app} and E^{app} as a function of the volume size V. As expected, the dispersion of the results decreases when the size of the domain increases for all used boundary conditions. The obtained mean values generally depend on the volume size, but also on the type of boundary conditions. For each modulus, the values converge towards the same limit for large volumes V, that are called here k^{eff} and μ^{eff}, since they are good candidates to coincide with the wanted effective properties. The values k^{eff} and μ^{eff}, found for large volume sizes, are reported in Table 5 and compared to the Voigt–Reuss (upper bound and lower bound), Hashin–Shtrikman bounds (HS+ and HS−) and self-consistent estimate. The self-consistent model (SC), also given in Table 5, provides a fair estimate for specimen SA$_2$. However, it strongly overestimates the effective properties of specimen SB$_1$. For small volumes, the average moduli obtained by simulations depend on the boundary conditions: KUBC produce results close to the upper bound. The mean value given by the periodic boundary conditions converge more rapidly towards the constant values k^{eff}, μ^{eff}, compared to the other boundary conditions. It turns out also that for sufficiently large sizes, here around: $V = 13,824$ μm^3, the mean value obtained with the periodic boundary condition practically does not depend on the size of simulations. It is claimed, in several works, [38,22,21], that the periodic boundary conditions provide the most reasonable estimates among the class of possible boundary conditions for statistically homogeneous media. There is however no formal proof of this fact.

Figs. 7 and 8 also give the corresponding interval of variation $[\overline{Z} - 2D_Z, \overline{Z} + 2D_Z]$, where Z is the apparent property, $\overline{Z}$ its average value and D_Z^2 its variance of estimation for n realizations. It can be noted that the mean apparent properties obtained with periodic boundary conditions on regular partitions of the sample or on random domains are very close. The variance obtained with the regular partition is larger than for the random sampling. This may be due to the fact that a random sampling does not cover the entire volume contrary to the regular partition.

5.1.2. Thermal conductivity

The specimens SA$_1$ and SB$_2$ are used now to estimate the apparent thermal properties. The results of numerical simulations are given only for periodic boundary conditions, and compared to the results found directly on the whole samples with homogeneous boundary conditions (UHF and UGT). Fig. 9 gives the obtained mean values and variances of the apparent thermal conductivity found in direction (OX) as a function of the volume size. The value of λ^{eff} found for large volume sizes is reported in Table 5 and compared to the Wiener and Hashin–Shtrikman bounds. The value λ^{eff} lies between the values found using the boundary conditions UGT and UHF (Fig. 9). It can be noticed again that the self-consistent model gives a fair estimate for SA$_2$ but overestimates strongly SB$_1$.

5.2. Determination of integral ranges

Following the strategy proposed in [21], the information gathered about the evolution with the volume V of the scatter of simulated apparent properties is used to identify the statistical volume parameter A_3 called integral range, which
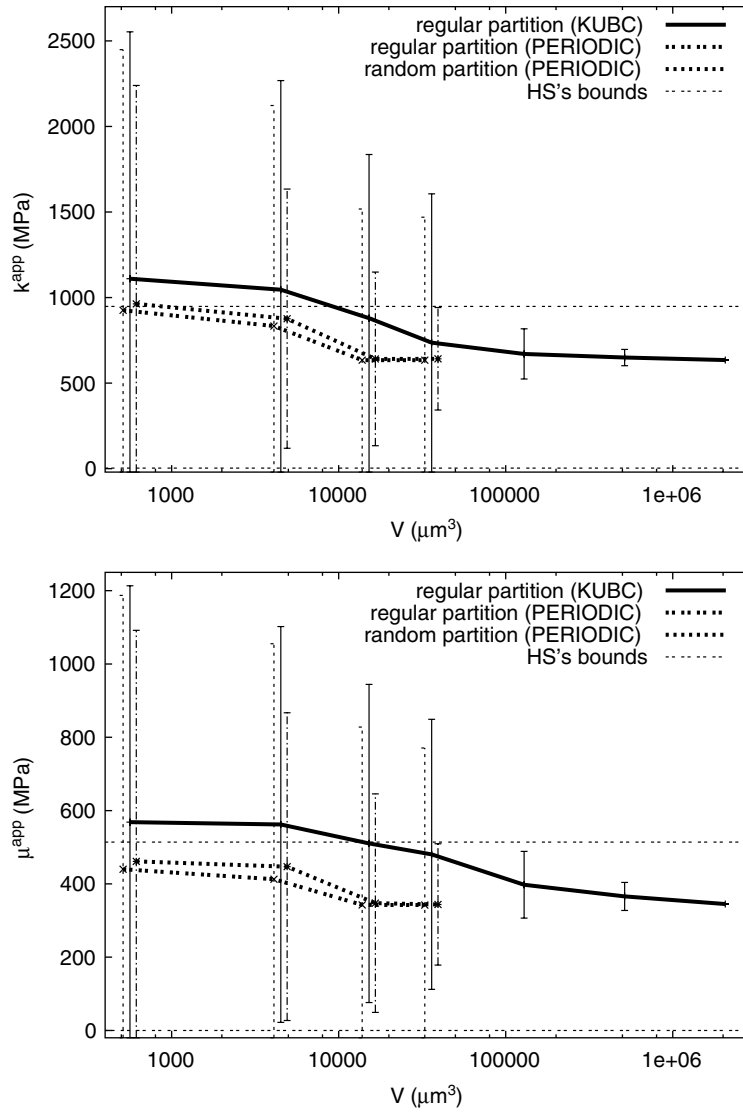
Fig. 8. Mean values and intervals of variation on the mean value for k^{app} and for μ^{app} as a function of domain size for the specimen SA$_2$.

Table 5
Values of numerical results (simulated on domains with volume $V = 32,768\ \mu m^3$), Voigt–Reuss or Wiener bounds (upper and lower bounds), Hashin–Shtrikman bounds (HS+, HS−) and self-consistent estimate (SC) for elastic and thermal properties for the specimens SA$_2$ and SB$_1$

Property	Simulation	Upper bound	Lower bound	HS+	HS−	SC
μ (SA$_2$)	345	660	0.05	514	0.11	371
μ (SB$_1$)	207	702	0.06	564	0.13	456
k (SA$_2$)	634	1430	2.65	948	2.70	618
k (SB$_1$)	334	1521	3.08	1058	3.14	791
λ (SA$_2$)	1.20	1.68	0.08	1.46	0.17	1.31
λ (SB$_1$)	0.77	1.79	0.09	1.58	0.20	1.47

The elastic moduli are given in MPa, the thermal conductivity in (W m^{-1} K^{-1}). The experimental value of λ for SB$_1$ is 0.85 (W m^{-1} K^{-1}).

will enter the definition of a representative volume element size. This is done successively for elastic and thermal properties.

5.2.1. Elastic moduli

The effective properties are defined from spatial averages of fields over a volume V. The fluctuations of the average values over different realizations of the real microstructures inside the volume V are considered. If the apparent property Z is
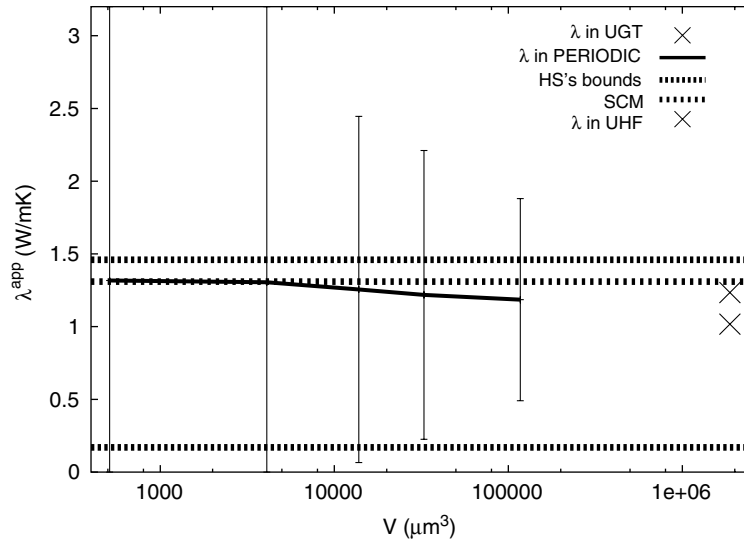
Fig. 9. Mean values and intervals of variation on the mean value for thermal conductivity, as a function of the domain size for the specimen SA$_2$.

obtained by averaging an additive scalar over the volume V, it is shown in [27] that, for asymptotically large volumes, the variance $D_Z^2(V)$ of $Z(V)$ is given by

$$D_Z^2(V) = D_Z^2 \frac{A_3}{V}.$$ (42)

A similar relation was proposed and tested by [8] and in [21]. In the case of a two-phase material with elastic property Z_1 for phase 1 and Z_2 for phase 2, the point variance D_Z^2 of the random variable Z is given by

$$D_Z^2 = P_1(1 - P_1)(Z_1 - Z_2)^2.$$ (43)

Since the apparent bulk and shear moduli are defined by the mean elastic strain energy for a given applied overall strain tensor, the asymptotic relation (42) applies to these elastic properties. Using Eq. (43) and the elastic properties of the constituents of the material studied in this work (1), we have: $D_k^2 = 933,784$ MPa^2, $D_\mu^2 = 198,988$ MPa^2 in the case of the specimen SA$_2$ and $D_k^2 = 855,978$ MPa^2, $D_\mu^2 = 181,680$ MPa^2 in the case of the specimen SB$_1$. The integral range A_3 remains then to be identified by fitting our data to Eq. (42) for k^{app} and μ^{app}. Such an identification is allowed only for domain sizes such that the mean property is not biased any more. It happens to be the case for periodic boundary conditions when $V > 10,000$ μm^3, according to Fig. 8. The found parameter A_3 (in μm^3) is given in Table 6. The values were identified from the dispersion of apparent properties in volumes with different sizes extracted randomly from the whole samples (actually the two volumes for which no bias is observed on the mean values). The value of the integral range is comparable to the size of the microstructural heterogeneities defined as the covariance range (Fig. 2): the elastic fields and the microstructure of the specimen SB$_1$ show a larger range. The largest integral range of the elastic moduli is found for the shear modulus in both microstructures. This must be related to the fact that the contrast in shear modulus between phases 1 and 2 is higher than for the bulk modulus.

5.2.2. Thermal conductivity

The model (42) proposed in the case of elastic properties can be used also for apparent thermal properties, since the apparent thermal conductivity is computed as the mean value $\langle q_i G_i \rangle$ for a prescribed vector $G_i = \delta_{i1}$. The point variance

Table 6
Values of the integral range A_3 for elastic moduli k and μ and thermal conductivity λ in the case of periodic boundary conditions for the specimens SA$_2$ and SB$_1$

Physical properties	Integral range A_3 (μm^3)
μ (SA$_2$)	1318 ± 11
μ (SB$_1$)	3156 ± 26
k (SA$_2$)	866 ± 4
k (SB$_1$)	2063 ± 37
λ (SA$_2$)	8510 ± 257
λ (SB$_1$)	8910 ± 331

is $D_\lambda^2 = 1.2560$ (W m^{-1} K^{-1})^2 in the specimen SA$_2$ and $D_\lambda^2 = 1.1498$ (W m^{-1} K^{-1})^2 for the specimen SB$_1$. The values of the integral range A_3 identified from the simulations (periodic boundary conditions) is given in Table 6. The largest integral range for the thermal conductivity is obtained for the specimen SB$_1$ (as for the elasticity), but the two values are rather similar. It is worth noting that the integral range found for thermal properties is larger than the value found for elastic properties.

5.3. Estimating RVE sizes

The real microstructures studied here can be considered as realizations of a random set. The size of a RVE must be given for a specific physical or morphological property, a given contrast in this property in different phases, and a given precision in the estimation of the effective studied property. It is recalled that, in the theory of samples, the absolute error ϵ_{abs} and relative error ϵ_{rel} on the mean value of a studied property Z, obtained with n independent (different) realizations of volume V, are given as functions of the variance $D_Z(V)$ by

$$\epsilon_{abs} = \frac{2D_Z(V)}{\sqrt{n}}, \quad \epsilon_{rel} = \frac{\epsilon_{abs}}{\overline{Z}}. \tag{44}$$

The size of the RVE can be defined formally as the volume V_{RVE} for which $n = 1$ realization is necessary and sufficient to estimate the mean (effective) property Z with a relative error $\epsilon_{rel} = 1\%$ for instance, provided we know the function $D_Z(V)$. On the other hand, we can estimate the effective property using smaller volumes, and consider n different realizations to obtain the same relative error ϵ_{rel}. Eq. (44) gives

$$n = \frac{4D_Z^2(V)}{\overline{Z}^2 \epsilon_{rel}^2}, \tag{45}$$

where Z stands here for k^{app}, μ^{app} or λ^{app}. The exact mean value $\overline{Z}$ and its variance for a given domain size are a priori unknown in the case of effective elastic moduli and effective thermal conductivity. The variance $2D_Z(V)$ of the mean value is given by Eq. (42) and can be inserted in Eq. (45). The smallest volume necessary and sufficient for the estimation of the effective property Z with a given absolute error ϵ_{abs} and n simulations is then

$$V^{RVE} = \frac{4}{\epsilon_{abs}^2} D_Z^2 \frac{A_3}{n}. \tag{46}$$

The absolute error ϵ_{abs} corresponds to the estimation of the mean apparent moduli $\overline{Z^{app}}$ which have been found to depend in general on domain size and do not necessarily coincide with the wanted effective property Z^{eff}, especially for small domain sizes and uniform boundary conditions (KUBC and SUBC) (UGT and UHF in thermal conductivity). This corresponds to a bias of the estimation. From the results of Figs. 7 and 8, the smallest domain size for which the bias can be neglected is about $V = 13,824$ µm^3 for k^{app}, μ^{app} and λ^{app} in the case of periodic boundary conditions for both types of microstructures. For the uniform boundary conditions, significantly larger volumes are needed (the whole volume of microstructure: $250 \times 250 \times 30$ µm^3 at least) to obtain unbiased mean values, i.e. mean apparent moduli $\overline{Z^{app}}$ that almost coincide with the wanted effective ones Z^{eff}.

One can now define the minimum size of the RVE, V^{RVE}, for a given ϵ_{rel} and a given number $n = 100$ of fields (for instance). When $\epsilon_{rel} = 1\%$, the values of V^{RVE} for both types of studied microstructures and for all the physical properties (k, μ and λ) are given in Table 7. For the same relative precision and number of fields, the thermal conductivity requires a volume larger than the volume required for the shear modulus and the bulk modulus although the contrast in shear modulus is the largest one. This result holds for both specimens. One must note also that the specimen SB$_1$ requires a volume larger than the volume required by the specimen SA$_2$. This is due to the values of the integral ranges and the covariance ranges, and this result is true for k, μ and λ.

Finally, the estimated RVE sizes must be compared to the actual size of the samples. The representative volumes predicted by the previous model are given in Table 7. It appears clearly that the samples SA$_i$ can almost be regarded as RVEs

Table 7
The minimal size of the RVE V^{RVE} for different physical properties obtained by the periodic boundary conditions

Sample SA$_2$	Sample SB$_1$
$V_k^{RVE} = 93 \times 93 \times 93$ µm^3	$V_k^{RVE} = 185 \times 185 \times 185$ µm^3
$V_\mu^{RVE} = 96 \times 96 \times 96$ µm^3	$V_\mu^{RVE} = 175 \times 175 \times 175$ µm^3
$V_\lambda^{RVE} = 162 \times 162 \times 162$ µm^3	$V_\lambda^{RVE} = 186 \times 186 \times 186$ µm^3

The results are given for $n = 100$ and $\epsilon_{rel} = 1\%$.

for the bulk and shear moduli (but not for thermal conductivity). However, the thickness remains too small and one would need more that three samples to ensure a precision of 5%. The samples SB_i are definitely too small, so that the proposed values for k^{app}, μ^{app} and λ^{app} remain estimations with loose precision.

6. Strain localization and percolation phenomena

The objective of this part is to understand from the morphology of the microstructures and the local fields in deformed samples, why the samples of material A have been found to be significantly stiffer than the material B. The previous sections have drawn the attention on the fact that the covariance and integral ranges are larger for material B than for material A. This features explain why the size of the RVE for a given precision will be larger for B than for A. But it does not give any information on the morphological or mechanical aspects that are responsible for the significantly larger stiffness of material A. The stiffness of the mixture of highly contrasted phases is strongly related to the way the hard phase percolates inside the material. In the next sections, notions of geometrical and mechanical percolations are defined. The mathematical description of the percolation is associated with the notion of percolation threshold, or critical value of the volume fraction describing the connectivity. A more general definition is necessary in the context of the mechanics of heterogeneous media. Contrary to the initial naive view of percolation mainly based on binary arguments ("percolate or not"), percolation can be seen as a continuous process in the case of continuous systems, and not necessary an abrupt one. With the help of tools of image analysis and of the morphological process called image reconstruction, such a notion is introduced and applied to the morphology of the hard phase investigated in this paper, on the one hand, and to mechanical fields (strain) to quantify strain localization phenomena on the other hand. A percolation ratio is defined and determined in each case. A correlation is drawn with the corresponding mechanical properties of the microstructures.

6.1. Percolation ratio

A quantitative parameter is necessary to compare how a given phase percolates inside different heterogeneous materials. For that purpose, we use the notion of 3D image reconstruction. Let us consider the set Y, subset of a larger set X. The geodesic dilatation with size l of Y in X is $D_X^l(Y) = \{x \in X, d_X(x, Y) \leqslant l\}$, $d_X(x, Y)$ being the smallest geodesic distance $d_X(x, y)$ between the point x and any point $y \in Y$. It is recalled that the geodesic distance $d_X(x, y)$ is the length of the shortest path in X connecting the points x and y. We define the geodesic re-construction by successive geodesic dilatations with size $l = 1$ pixel of Y in X, until the whole set X has been explored.

The volume fraction P_p of phase P percolating in direction (OX) is defined by the following procedure:

1. Determine the 3D reconstruction of the first section $x = 1$ (pixel) of the image of phase P in direction (OX). Call it P_p^x.
2. Determine the 3D reconstruction of the last section $x = 512$ (pixel) of the image of phase P in direction $(-OX)$. Call it P_p^{-x}. $-x$ means that the propagation obtained from the successive dilatations is made in the opposite direction of (OX).
3. The percolating phase in (OX) direction is then defined as the intersection of P_p^x and P_p^{-x}: $P_p = P_p^x \cap P_p^{-x}$.

It is clear that the volume fraction of percolating phase P_p is lower than or equal to the volume fraction of phase P studied in the heterogeneous material. It enables us to quantify the volume of phase that "percolates" inside the volume X and to compare it to the whole volume of this phase. It is then possible to define a *percolation ratio* P_r, as the ratio between the volume fraction of the percolating phase to the whole volume fraction in the microstructure of this phase:

$$P_r = \frac{P_p}{P}. \tag{47}$$

It is always lower than or equal to 1. It is equal to 1 if the whole phase percolates, and equal to zero if there is no percolation of this phase (physically it means that this phase is a set of separate inclusions). Fig. 10 illustrates the three steps in the 2D image reconstruction. This procedure is used in 3D in the sequel. The proposed parameter makes it possible to determine the inclusion character of a given phase, in a way which can be shown to be more reliable than for instance the so-called "matricity coefficient" introduced in [24].

6.2. Geometrical percolation

The previous definition of percolating phase P_p substantiates the notion of geometrical percolation. In particular, we will say that the phase P geometrically percolates in the considered volume as soon as the volume fraction of percolating phase P_p does not vanish. Because of the size of the investigated samples SA_i and SB_i, especially their small thickness with respect to the (OZ) axis, we have chosen to study the evolution of the geometrical percolation ratio for the phases 1 and 2, as a function of the number sections (XY) added in the thickness direction (OZ). For each number m of sections included in
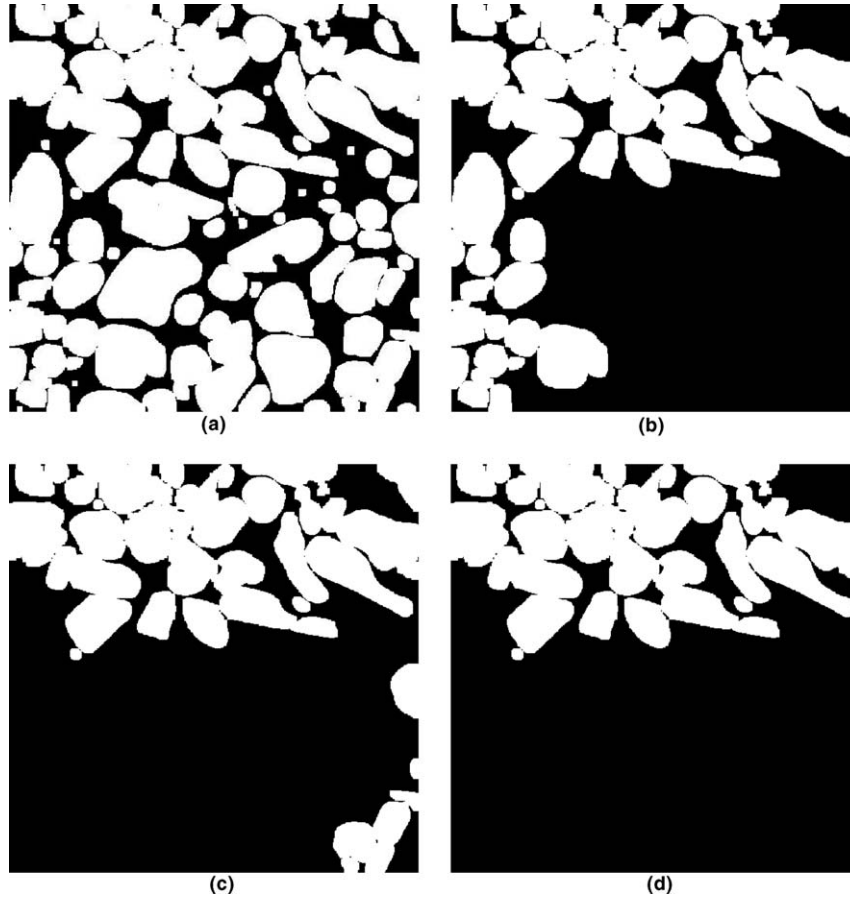
Fig. 10. Example of 2D image re-construction. (a) Image of the whole set X, (b) image of P_p^x, (c) image of P_p^{-x} and (d) image of P_p.

the 3D image, the geometrical percolation ratio $P_r(m)$ is computed in two directions of sections (OX) and (OY). The obtained curves are given in Fig. 11. For $m = 1$, the performed image analysis is two-dimensional, as illustrated in Fig. 10.

6.2.1. Material A

The evolution of the geometrical percolation ratio P_r in direction (OX) with increasing thickness, is given in Fig. 11(a) for the phase 1 in the three samples SA_i. The number of sections added along the thickness is equal to 60 for a total thickness of 30 µm. In the first section of sample SA_2, the percolation ratio is zero, meaning that there is no path entirely contained in phase 1 that links both sides of the image in direction (OX). However, for all samples, the percolation ratio rises steeply with increasing image thickness and reaches the value 1. Such a value means that the entire phase 1 is connected within the considered volume. There is no isolated inclusion of phase 1. A sample thickness of 5 µm is sufficient for the percolation ratio to become larger that 0.95.

Very similar results are obtained for percolation in the direction (OY), and for the phase 2.

6.2.2. Material B

The percolation ratios for material B for a propagation in direction (OX) as functions of sample thickness are given for both phases 1 and 2 in Fig. 11(c) and (d) respectively. Again both phases are connected in all the samples SB_i. But the most salient feature is that the percolation distance, i.e. the minimal thickness for the percolation index to be larger than 0.95, is twice larger for phase 1 than for phase 2. A thickness of about 5 µm is necessary for the soft phase 2, whereas a value of about 13 µm is found for the hard phase 1. Such a result can be related to the fact that the covariance and integral ranges are about twice as large in material B as in material A. This specific morphological property of the phase 1 is in accordance with the direct observation of the images of Fig. 1 where the heterogeneities made of the hard phase are indeed larger than the channels made of phase 2.

Very similar results are obtained for percolation in the direction (OY).

At this stage, there is a strong correlation between this difference in the percolation behaviour of phase 1 in both materials and the found mechanical properties of materials A and B. However, it is not possible to prove a direct link between
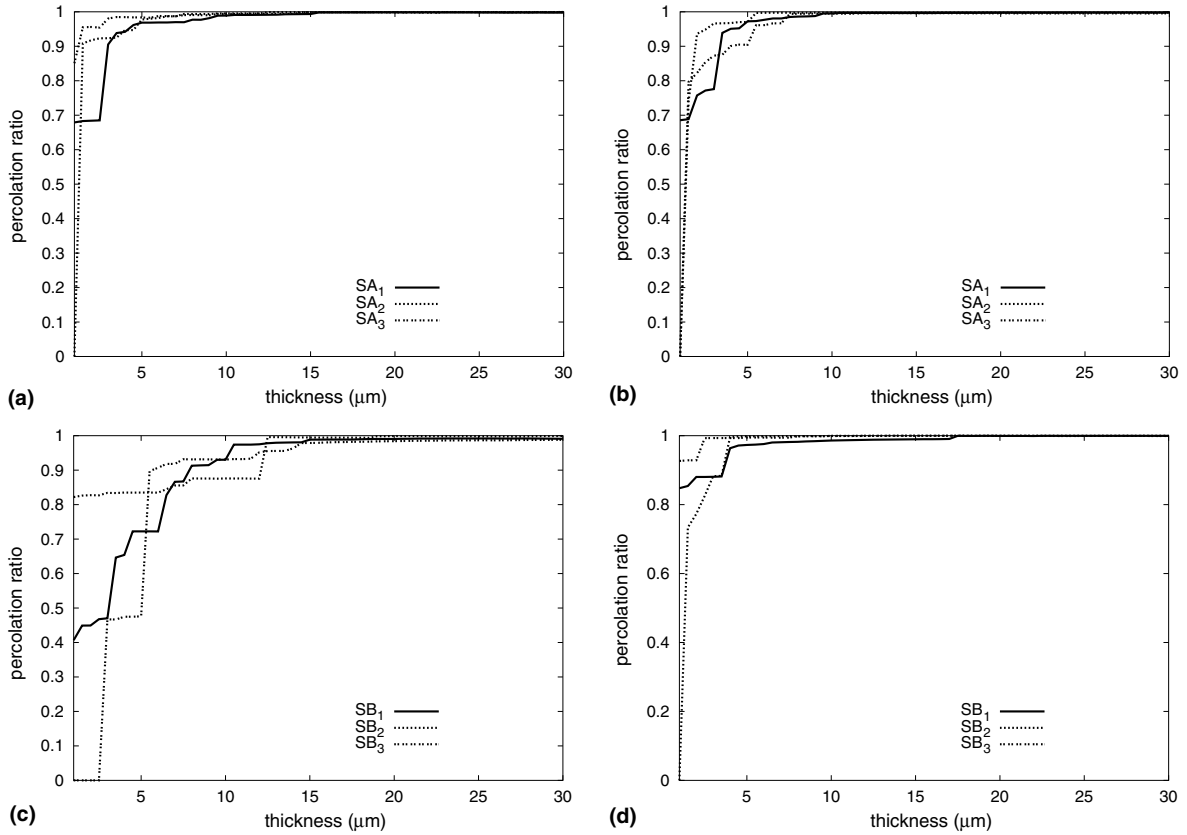
Fig. 11. Evolution of the geometrical percolation ratio P_r in direction (OX) as a function of sample thickness: (a) material A for the phase 1, (b) material A for the phase 2, (c) material B for the phase 1 and (d) material B for the phase 2.

the percolation distance of phase 1 in material A and the found high elastic moduli. To go a step further, a notion of mechanical percolation is introduced in the next section.

6.3. Mechanical percolation

The objective is to study the geometry of zones of high strain or high stress in a microstructure submitted to a given load. The size and morphology of strain localization zones for instance can be very different from material to material. Strain localization bands connecting one face of the sample to the other can weaken the material considerably more than bounded domains inside the sample. That is why the percolation behaviour of the geometrical domain where strain or stress reach a given value is investigated.

The percolation of a mechanical field in a given direction is defined as follows: a value of a mechanical variable (ε_{eq} for instance, defined by Eq. (24)) is attributed to each voxel of the microstructure according to the results of a finite element computation. A threshold image is obtained by selecting the domain where the variable is greater than a given threshold. One investigates then the geometrical percolation property of this domain. In particular the percolation ratio can be computed in the same way as in the previous section.

This procedure is applied to the samples SA_1 and SB_1 subjected to an external loading $E_{22} = 0.1$ using KUBC. The chosen local variable is the equivalent strain ε_{eq}. This local variable strongly varies in the microstructure. For a given value ε^{thres}, the part $\mathscr{D}_{\varepsilon^{thres}}$ of the image where $\varepsilon_{eq} > \varepsilon^{thres}$ is determined. One computes then the geometrical percolation ratio $P_r(\mathscr{D}_{\varepsilon^{thres}})$ of this domain in one specific direction, according to the definition (47). We call it the mechanical percolation ratio of the equivalent strain field $\varepsilon_{eq}(\underline{x})$ in a given direction and for a given threshold.

Fig. 12(a) and (b) give examples of the percolating domain of the equivalent strain for samples SA_1 and SB_1 respectively. They show the domains of the microstructure where the equivalent strain is larger than $\varepsilon^{thres} = 0.4$ for the sample SA_1 and than $\varepsilon^{thres} = 0.5$ for the sample SB_1, and that percolate geometrically in direction (OX). Fig. 12(a) and (b) are deduced from the whole equivalent strain maps of Fig. 3(a) and (b) respectively. Fig. 13 shows then the mechanical percolation ratio as a function of threshold value ε^{thres}, in direction (OX) (loading is along direction (OY)), for materials A and B respectively. It is clear that the mechanical percolation ratio is equal to 1 for very low threshold values and vanishes for high values.
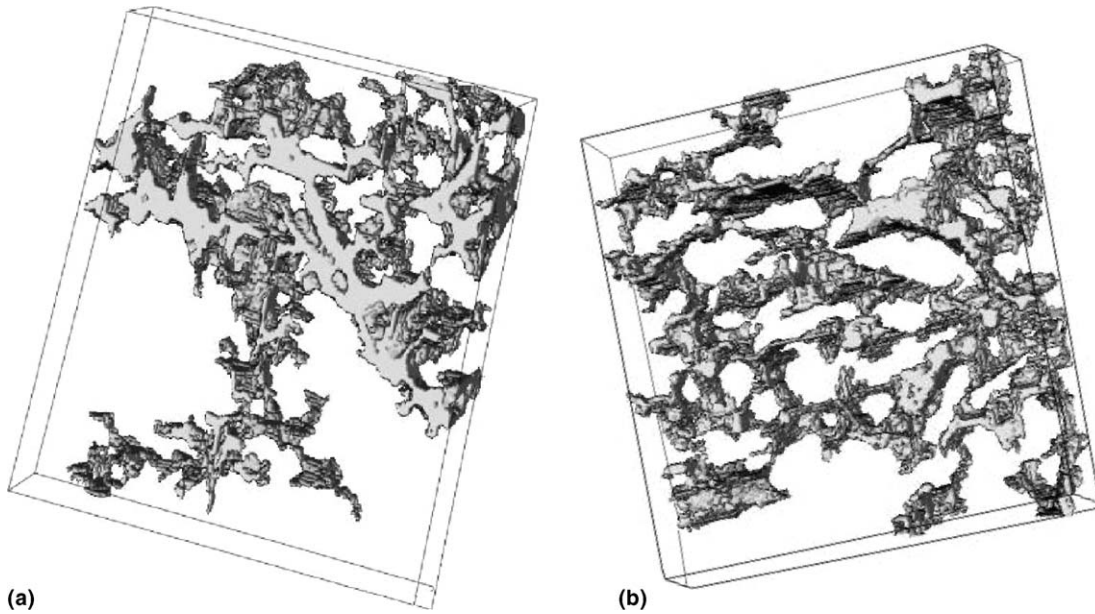
(a)   **(b)**

Fig. 12. Image of the percolated volume P_p for the variable ε_{eq} for the computation using the sample (a) SA_1. The imposed strain tensor is $E_{22} = 1$. The percolation is given in the direction (OX), $\varepsilon_{eq} = 0.4$ ($P_r = 0.74$). (b) Image of the percolated volume P_p for the variable ε_{eq} for the computation using the sample SB_1. The imposed strain tensor is $E_{22} = 1$. The percolation is given in the direction (OX), $\varepsilon_{eq} = 0.5$ ($P_r = 0.95$).
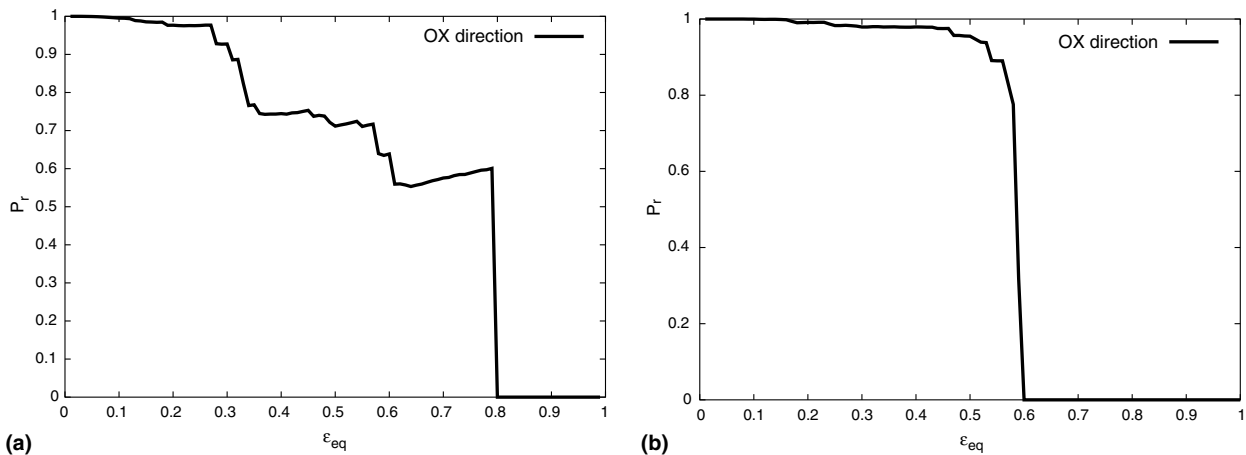

(a)   **(b)**

Fig. 13. Evolution of the strain field percolation ratio as a function of the equivalent strain threshold: (a) example of computation of the sample SA_1 with $E_{22} = 0.1$ and (b) computation of the sample SB_1 with $E_{22} = 0.1$.

However, the way the mechanical percolation ratio decreases as a function of ε^{thres} is very different for samples SA_1 and SB_1. It decreases slowly for sample SA_1 and abruptly for sample SB_1. It indicates that high strain domains can percolate for a higher strain in specimen SA_1, as compared to specimen SB_1. It can also be related to the fact that the higher deformations develop in a more localized way in the soft phase of sample SB_1. A complementary information could be obtained by a similar approach, when considering the sets generated by $\varepsilon_{eq} < \varepsilon^{thres}$. This would inform us about the percolation and the localization of domains with the lower strains.

7. Conclusions

Confocal images of two materials having the same volume fraction of hard phase 1 but different morphologies, have been used to predict their effective elastic and thermal properties. Direct finite element simulations on the six available samples SA_i and SB_i show that the apparent properties obtained using KUBC and SUBC boundary conditions are significantly different. The results obtained with SUBC are closer to the experiment. This discrepancy is due to the finite size of the samples, and especially their small thickness. A method is proposed then to estimate the size of a proper RVE for a given

wanted precision. It is based on the computation of material volumes of increasing size extracted from the whole samples. The finite element simulations using periodic boundary conditions provide apparent moduli that converge rapidly towards an asymptotic value which is regarded here as the effective property for increasing volume size. A sufficiently large number of volumes must be selected inside the whole sample to reach a given precision on the estimation of the mean. The evolution of the variance in apparent moduli with increasing volume is given by Eq. (42), where the parameter A_3 called integral range has been identified for elastic and thermal properties. This key-parameter makes it possible to estimate RVE sizes for given precision and number of considered volumes, according to Eq. (45). When applied to the materials A and B, this approach shows that the samples SA$_i$ are RVE for a precision of 5%, whereas the samples SB$_i$ are too small to reach this precision. This feature can be related also to the values of covariance ranges which characterize the size of heterogeneities. Such a methodology is an efficient and systematic tool to assess the representativity of the 3D images that are produced by modern experimental techniques like X-ray tomography. The integral range can be used to compare RVE sizes of different materials for different properties. In the considered materials A and B, the integral range for the shear modulus is larger than for the bulk modulus. Furthermore the integral range for thermal property was found to be significantly larger than for elastic properties.

The existence of the asymptotic behaviour (42) in the scatter of apparent properties makes it possible to extrapolate results from a finite domain of material to larger volume based on the integral range A_3, and therefore to predict the required volume size of materials needed for proper identification of effective properties. A condition for the identification of A_3 from computations on small volumes extracted from a larger one is that the computed mean apparent properties do not vary significantly with volume size and therefore represent a fair estimate of the effective property. This prerequisite is not fulfilled when using homogeneous boundary conditions but was found to be satisfied if periodic boundary conditions are prescribed. The strong advantage of periodic boundary conditions even for random materials was already noticed at several places [21,32] and is put forward in the present work for the analysis of real microstructures. However, the periodic boundary conditions also lead to significant scatter in the found apparent properties. That is why we have proposed to randomly select a high enough number of subvolumes inside the reference images to ensure a given precision in the estimation of the mean apparent properties. This is in contrast to the alternative computation homogenization approach based on regular and non-overlapping partitions of the reference material volume V into subvolumes subjected to homogeneous boundary conditions, as done for instance in [44].

The finer and elongated microstructure of material A leads to stiffer elastic properties and higher thermal conductivity than material B. The entanglement of the hard phase 1 within the material plays an important role in the resistance of both materials. A quantitative notion of percolation is introduced in this work. The geometrical percolation ratio in a given spatial direction characterizes the volume fraction of one phase that is actually connected to both faces normal to the direction in the considered volume. It turns out that this ratio is equal to 1 for the hard phase in all available samples, which means full percolation of phase 1 in both materials. However, geometrical percolation is a fully 3D parameter. A percolation distance could be defined that characterizes the minimum sample thickness for the percolation ratio to reach 0.95. This percolation distance is twice as large in material B as in material A. There seems to be a correlation between this percolation behaviour of the hard phase and the resulting mechanical properties. In addition, a notion of mechanical percolation was introduced in order to substantiate this correlation. The proposed analysis indicates that in a deformed sample, high strain domains are connected for larger strains for microstructure A than for microstructure B. These are first links between morphological and mechanical analyses which remain however insufficient to unambiguously distinguish microstructure A from B. The percolation indices proposed and illustrated in this work are thought to be more efficient and systematic than available parameters like the matricity index used for instance in [35]. Further efforts towards reconciliation of morphological and mechanical/physical approaches are necessary to really understand, classify and finally optimize 3D microstructures.

References

[1] P. Adler, C. Jacquin, J. Quiblier, Flow in simulated porous media, Int. J. Multiphase Flow 16 (1990) 691–712.
[2] P. Adler, C. Jacquin, J.-F. Thovert, The formation factor of reconstructed model three-dimensional porous media, Water Resour. Res. 28 (1992) 1571–1576.
[3] F. Barbe, L. Decker, D. Jeulin, G. Cailletaud, Intergranular and intragranular behavior of polycrystalline aggregates. Part 1: F.E. model, Int. J. Plast. 17 (2001) 513–536.
[4] D. Bergman, The dielectric constant of a composite material, a problem in classical physics, Phys. Rep. 43 (1978) 377–407.
[5] J. Besson, G. Cailletaud, J.L. Chaboche, S. Forest, Mécanique non linéaire des matériaux, Hermès Science, 2001.
[6] F. Bron, D. Jeulin, Modeling a food microstructure by random sets, Image Anal. Stereol. 23 (2004) 33–44.
[7] G. Cailletaud, S. Forest, D. Jeulin, F. Feyel, I. Galliet, V. Mounoury, S. Quilici, Some elements of microstructural mechanics, Comput. Mater. Sci. 27 (2003) 351–374.
[8] G. Cailletaud, D. Jeulin, P. Rolland, Size effect on elastic properties of random composites, Engrg. Comput. 11 (1994) 99–110.
[9] U.R. Colworth, Unilever Laboratory Progress Report, Unilever Research Colworth, 2000.
[10] A. Elvin, Number of grains required to homogenize elastic properties of polycrystalline ice, Mech. Mater. 22 (1996) 51–64.

[11] F. Feyel, J.-L. Chaboche, FE^2 multiscale approach for the modelling of the elastoviscoplastic behavior of long fibre SiC/Ti composites materials, Comput. Methods Appl. Mech. Engrg. 183 (2000) 309–330.

[12] B. Flannery, H. Deckman, W. Roberts, K. Damico, Three-dimensional X-ray microtomography, Science 237 (1987) 1439.

[13] J. Fredrich, B. Menendez, T. Wong, Imaging the pore structure of geomaterials, Science 268 (1995) 276–279.

[14] E. Garboczi, A. Day, An algorithm for computing the effective linear elastic properties of heterogeneous materials; three-dimensional results for composites with equal phase Poisson ratios, J. Mech. Phys. Solids 43 (1995) 1349–1362.

[15] Z. Hashin, Analysis of composite materials, J. Appl. Mech. 50 (1983) 481–505.

[16] S. Hazanov, C. Huet, Order relationships for boundary conditions effect in heterogeneous bodies smaller than the representative volume, J. Mech. Phys. Solids 42 (1994) 1995–2011.

[17] C. Huet, Application of variational concepts to size effects in elastic heterogeneous bodies, J. Mech. Phys. Solids 38 (1990) 813–841.

[18] C. Huet, Hierarchies and bounds for size effects in heterogeneous bodies. In: G. Maugin (Ed.), Proceedings of the Sixth Symposium on Continuum Moels and Discrete Systems, Dijon, 1989, vol. 2, 1991, pp. 127–134.

[19] P. Janssen, Modelling fat microstructures using finite element analysis, J. Food Engrg. 61 (2004) 387–392.

[20] D. Jeulin, M. Ostoja-Starzewski, Mechanics of Random and Multiscale Microstructures, Springer, 2001.

[21] T. Kanit, S. Forest, V. Mounoury, D. Jeulin, Determination of the size of the representative volume element for random composites: statistical and numerical approach, Int. J. Solids Struct. 40 (2003) 3647–3679.

[22] V. Kouznetsova, Computational Homogenization for the Multi-Scale Analysis of Multi-Phase Materials, Technische Universiteit Eindhoven, 2002.

[23] M. Kwiecien, I. Macdonald, F. Dullien, Three-dimensional reconstruction of porous sandstone from serial section data, J. Microsc. 159 (1990) 343–359.

[24] P. Leßle, M. Dong, E. Soppa, S. Schmauder, Simulation of interpenetrating microstructures by self-consistent matricity models, Scripta Mater. 38 (9) (1998) 1327–1332.

[25] N. Lippmann, T. Steinkopf, S. Schmauder, P. Gumbsch, 3D-finite-element-modelling of microstructures with the method of multiphase elements, Comput. Mater. Sci. 9 (1997) 28–35.

[26] E. Maire, A. Fazékas, L. Salvo, R. Dendievel, Y. Souhail, P. Cloetens, J. Letang, X-ray tomography applied to the characterization of cellular materials: related finite element modeling problems, Compos. Sci. Technol. 63 (2003) 2431–2443.

[27] G. Matheron, The Theory of Regionalized Variables and its Applications, Paris School of Mines Publications, 1971.

[28] M. Ostoja-Starzewski, Random field models of heterogeneous materials, Int. J. Solids Struct. 35 (19) (1998) 2429–2455.

[29] J. Poutet, D. Manzoni, F. Hage-chehade, C. Jacquin, M. Bouteca, J. Thovert, P. Adler, The effective mechanical properties of random porous media, J. Mech. Phys. Solids 44 (1996) 1587–1620.

[30] A. Roberts, M. Teubner, Transport properties of heterogeneous materials derived from Gaussian random fields: bounds and simulation, Phys. Rev. E51 (1995) 4141–4154.

[31] K. Sab, On the homogenization and the simulation of random materials, Eur. J. Mech. Solids 11 (1992) 585–607.

[32] K. Sab, B. Nedjar, Periodization of random media and representative volume element size for linear composites, C.R. Mécanique 333 (2005) 187–195.

[33] M. Sahimi, Flow, dispersion, and displacement processes in porous media and fractured rocks: From continuum models to fractals, percolation, cellular automata and simulated annealing, Rev. Mod. Phys. 65 (1993) 1393–1534.

[34] E. Sanchez-Palencia, A. Zaoui, Homogenization Techniques for Composite MediaLecture Notes in Physics No. 272, Springer, Berlin, 1987.

[35] S. Schmauder, U. Weber, I. Hofinger, A. Neubrand, Modelling the deformation behaviour of W/Cu composites by a self-consistent matricity model, Technische Mechanik, Band 19, Heft 4, 1999, pp. 313–320.

[36] L. Schwartz, F. Auzerais, J. Dunsmuir, N. Martys, D. Bentz, S. Torquato, Transport and diffusion in three dimensional composite media, Physica, A 207 (1993) 28–36.

[37] P. Spanne, J. Thovert, J. Jacquin, W. Lindquist, K. Jones, D. Coker, Synchotron computed microtomography of porous media: topology and transport, Phys. Rev. Lett. 73 (1994) 2001–2004.

[38] K. Terada, M. Hori, T. Kyoya, N. Kikuchi, Simulation of the multi-scale convergence in computational homogenization approaches, Int. J. Solids Struct. 37 (2000) 2285–2311.

[39] S. Torquato, Random heterogeneous media: microstructure and improved bounds on effective properties, Appl. Mech. Rev. 44 (1991) 37–76.

[40] S. Torquato, Random Heterogeneous Materials, Springer, 2002.

[41] T. Zohdi, Computational optimization of the vortex manufacturing of advanced materials, Comput. Methods Appl. Mech. Engrg. 190 (2001) 6231–6256.

[42] T. Zohdi, Constrained inverse formulations in random material design, Comput. Methods Appl. Mech. Engrg. 192 (2003) 3179–3194.

[43] T. Zohdi, P. Wriggers, Aspects of the computational testing of the mechanical properties of microheterogeneous material samples, Int. J. Numer. Methods. Engrg. 50 (2001) 2573–2599.

[44] T. Zohdi, P. Wriggers, C. Huet, A method of substructuring large-scale computational micromechanical problems, Comput. Methods Appl. Mech. Engrg. 190 (2001) 5639–5656.